

Topological synchronization of coupled nonlinear oscillators

Kazuki Sone,^{1,*} Yuto Ashida,^{1,2,3} and Takahiro Sagawa^{1,4}

¹*Department of Applied Physics, The University of Tokyo, 7-3-1 Hongo, Bunkyo-ku, Tokyo 113-8656, Japan*

²*Department of Physics, University of Tokyo, 7-3-1 Hongo, Bunkyo-ku, Tokyo 113-0033, Japan*

³*Institute for Physics of Intelligence, University of Tokyo, 7-3-1 Hongo, Tokyo 113-0033, Japan*

⁴*Quantum-Phase Electronics Center (QPEC), The University of Tokyo, 7-3-1 Hongo, Bunkyo-ku, Tokyo 113-8656, Japan*

Synchronization of coupled oscillators is a ubiquitous phenomenon found throughout nature. Its robust realization is crucial to our understanding of various nonlinear systems, ranging from biological functions to electrical engineering. On another front, in condensed matter physics, topology is utilized to realize robust properties like topological edge modes, as demonstrated by celebrated topological insulators. Here, we integrate these two research avenues and propose a nonlinear topological phenomenon, namely topological synchronization, where only the edge oscillators synchronize while the bulk ones exhibit chaotic dynamics. We analyze a concrete prototypical model to demonstrate the presence of positive Lyapunov exponents and Lyapunov vectors localized along the edge. As a unique characteristic of topology in nonlinear systems, we find that unconventional extra topological boundary modes appear at emerging effective boundaries. Furthermore, our proposal shows promise for spatially controlling synchronization, such as on-demand pattern designing and defect detection. The topological synchronization can ubiquitously appear in topological nonlinear oscillators and thus can provide a guiding principle to realize synchronization in a robust, geometrical, and flexible way.

Nonlinear oscillators ubiquitously appear in a variety of fields from biology [1, 2] to engineering [3–6]. They often exhibit synchronization [7], where (even inhomogeneous) interacting oscillators vibrate at the same frequency. Synchronization plays a crucial role in classical nonlinear systems, e.g., circadian rhythm [8], and even in quantum systems [9, 10]. Controlling synchronization and desynchronization [11–13] of nonlinear oscillators is essential to fulfill their functions. However, nonlinear oscillators are often irregularly affected by their uncontrollable circumstances, and therefore it is desirable to investigate universal principles to robustly control and design nonlinear oscillators against such disorder.

On another front, topology represents the property of matter unchanged under continuous deformations and thus can provide a guiding principle to realize robust systems. Numerous studies in condensed matter physics have focused on such utility of topology, where a remarkable example is a topological insulator [14, 15] exhibiting a metallic surface and an insulating bulk. Topological insulators exhibit topologically nontrivial bulk associated with edge-localized modes robust against disorder, as a consequence of a principle called bulk-edge correspondence [15]. Such edge modes exhibit gapless dispersion relations and backscattering-free edge current. Because bulk topology is intrinsically related to Hamiltonians that govern linear dynamics, topology in physics has been studied mostly in linear systems. In recent studies, it has been revealed that topological edge modes can affect the nonlinear dynamics [16, 17] in, e.g., photonics [18] and mechanical lattices [19], where topological edge soliton [20] and bulk-localized topological modes [21] can emerge. Despite these recent advancements, topology in nonlinear systems is still largely unexplored even at the conceptual level.

Given these fundamental problems, we here propose a topological mechanism of robust edge-localized synchronization, where only nonlinear oscillators at the edge of the system synchronize, whereas dynamics of the bulk oscillators is chaotic.

We demonstrate the emergence of such a synchronized state by numerical calculations of nonlinear oscillators with linear couplings corresponding to a topological Hamiltonian. We term the proposed state as a topological synchronized state (TSS). By calculating the Lyapunov exponents [22] and vectors [23, 24], we confirm the chaotic behavior of bulk oscillators and find that topological edge modes are represented by the edge-localized Lyapunov vectors. While such coexistence of synchronization and desynchronization is apparently reminiscent of chimera states [25–32], we emphasize that the mechanism of the proposed TSS is distinct from conventional chimera states because of its topological origin. Moreover, nonlinearity leads to another unique topological phenomenon: unconventional extra boundary modes appear at the emergent effective boundary. Such extra boundary modes can increase the number of synchronized oscillators in the TSS. As applications of the TSS, we propose to arrange the synchronized oscillators in an on-demand pattern, and to detect defective structures by observing the lasing patterns around the defects. We also propose a concrete electrical-circuit realization of the TSS. While we focus on several types of non-Hermitian Hamiltonians [33–38] of lasing edge modes [39–41] to realize the TSS, we expect that the TSS can ubiquitously emerge in nonlinear oscillators with topological linear couplings. In addition, the robustness of the topological edge modes guarantees the stability of the TSS against detuning parameters and thus provides a robust and universal mechanism to control synchronization.

Model of topological synchronization and its dynamics.— We consider coupled nonlinear oscillators that self-vibrate even if they are decoupled. Such oscillators maintain their self-oscillations at the balance of the injection and dissipation of energy and exhibit nonlinear features that cannot arise in linear harmonic oscillators, such as the robustness of the amplitude. Dynamics of nonlinear oscillators can be described as a limit cycle; one of the simplest models for this

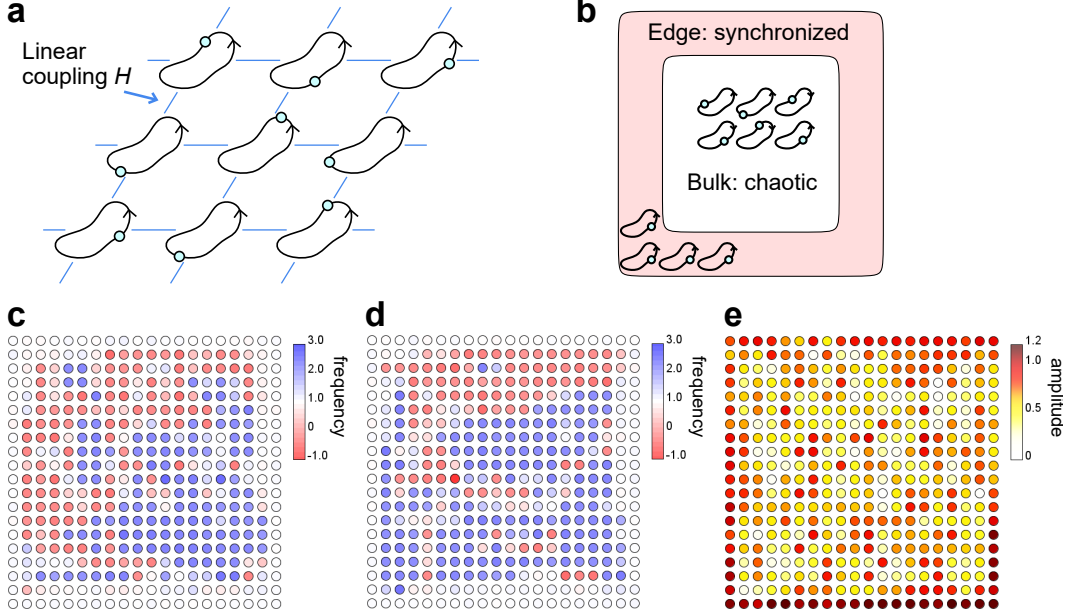


FIG. 1. Dynamical formation of topological synchronized states (TSSs). **a** Nonlinear oscillators are placed on a square lattice. Each oscillator is linearly coupled to other oscillators at the nearest neighbor sites. The linear coupling corresponds to the Hamiltonian of a topological insulator laser, which exhibits amplified edge oscillations. **b** The TSS can be observed under the open boundary condition. The nonlinear oscillators near the boundary synchronize, while those away from the boundary exhibit chaotic dynamics instead of being synchronized. **c, d** The frequency of the first component of oscillators at each site is presented. We numerically calculate the dynamics of the first model of the TSS (Eq. (1)). Panel **c** (**d**) is the snapshot at the time $t = 100$ ($t = 200$). Empty sites represent the oscillators oscillating around their natural frequencies. We confirm that the frequencies of the edge oscillators are almost homogeneous and constant, which indicates their synchronization. Meanwhile, the oscillators inside exhibit inhomogeneous frequencies. One can also confirm that their frequencies vary over time, thus indicating the desynchronization and instability of the bulk oscillators. The parameters used are $u = -1$, $b = 0.5$, $\alpha = 0.5$, $\beta = 1$, $\omega_0 = 1$, and $\Delta\omega = 0.2$. **e** The amplitudes of the oscillators are shown. Here, we numerically simulate the dynamics of the model as in panels **c, d**. We check that the amplitudes of most of the edge oscillators are larger than those of the bulk oscillators. The same parameters as panels **c, d** are used in the calculation.

is the (complex) Stuart-Landau oscillators [42] described as $\dot{Z} = (i\omega + \alpha - \beta|Z|^2)Z$, where Z is the complex-valued state variable. Here, we focus on the case that β is real. This model exhibits self-excited oscillations with frequency ω and amplitude $\sqrt{\alpha/\beta}$ and is the normal form of a nonlinear oscillator around the parameters where it begins self-oscillations.

Topological synchronization of the edge oscillators can appear in coupled nonlinear oscillators where the linear coupling is described by a Hamiltonian that is topological in the wavenumber space. To construct a concrete model of the TSS, we consider linearly coupled Stuart-Landau oscillators arranged on a square lattice (see Fig. 1a). We assume that four oscillators exist at each site and they interact with ones at the same site as well as the nearest neighbor sites. The dynamics of our model is described by the following set of equations,

$$\frac{d}{dt} Z_j(\mathbf{x}) = (i\omega_j(\mathbf{x}) + \alpha - \beta|Z_j(\mathbf{x})|^2)Z_j(\mathbf{x}) - i \sum_{k, \mathbf{x}'} H_{jk}(\mathbf{x}, \mathbf{x}') Z_k(\mathbf{x}'), \quad (1)$$

where $\mathbf{x} = (x, y)$, $\mathbf{x}' = (x', y')$ represent the location of the site in the square lattice, and $j, k = 1, \dots, 4$ distinguish four oscillators at each site (four oscillators are necessary to real-

ize the desirable properties of the linear coupling, such as, its lasing edge modes discussed in the following). $H_{jk}(\mathbf{x}, \mathbf{x}')$ represents the linear coupling between the oscillators at the same site or the nearest neighbor sites. To investigate the robustness of the TSS against disorders, we introduce the inhomogeneity into the system such that natural frequencies of each oscillator, $\omega_j(x, y)$, are uniformly distributed around the mean value ω_0 with the distribution width being $\Delta\omega$.

To realize the TSS in a simple model, we first adopt the Hamiltonian of exceptional edge modes [41] as $H_{jk}(\mathbf{x}, \mathbf{x}')$ (see Supplementary Information for the detail), which utilizes the robustness of singularities called exceptional points, topological gapless structures unique to non-Hermitian systems. The exceptional edge modes are protected by the topology of the dispersion relations around their branchpoint structures [34] and exhibit lasing behavior [39, 40] amplifying edge oscillations. In nonlinear oscillators, such edge modes can lead to qualitatively different synchronization behavior between edge and bulk oscillators without judicious designing of the system.

We numerically calculate the dynamics of our model under the open boundary condition and confirm the emergence of the TSS, i.e., the synchronization (desynchronization) of the oscillators at the edge (in the bulk). Figures 1c,d show the

TABLE I. Summary of the properties of our models.

Model	TSS	Protection mechanism	Coupling	Nonlinearity-induced boundary modes
The first model (Supplementary Eqs. (S1), (S3))	Yes	Exceptional edge modes	Non-Hermitian	Yes
Model using conventional bulk topology (Supplementary Eq. (S4))	Yes	Conventional bulk topology	Non-Hermitian	No
Model using Hermitian linear couplings (Supplementary Eqs. (S14), (S15))	Yes (only 1st and 4th components synchronize)	Exceptional edge modes	Hermitian (Non-Hermiticity from nonidentical oscillators)	No

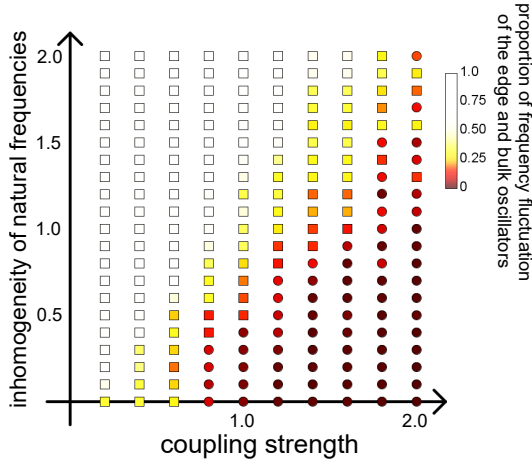


FIG. 2. Phase diagram of the model of the TSS. The ratio of frequency fluctuations of the edge oscillators to those of the bulk ones is depicted at each parameter. We calculate the dynamics of the model of the TSS (Eq. (1)) under different strengths of the linear coupling and the inhomogeneity of the natural frequencies. The red region (right bottom) shows parameter regimes where the TSS emerges. The circles and squares represent the classification of data of frequency fluctuations of the edge and bulk oscillators obtained by a numerical clustering method. The circles correspond to the parameters for which the presence of the TSS is identified. The phase boundary obtained here corresponds to the parameter points at which the bandgap of the effective Hamiltonian closes and thus the bulk band can change its topology.

frequency distribution obtained from the numerical simulations. One can see that the edge oscillators exhibit constant and homogeneous frequencies, indicating their synchronization, while the bulk ones oscillate at time- and space-varying frequencies. It is noteworthy that the fluctuations of natural frequencies are irrelevant to the TSS (see Supplementary Information for the related numerical calculation). The existence of TSS under the inhomogeneous natural frequencies indicates the robustness of TSS guaranteed by its topological nature. We carefully examine the robustness of TSS by calculating the dynamics of our model at different strengths of the

linear coupling and inhomogeneity of the natural frequencies. Figure 2 shows the phase diagram determined on the basis of frequency fluctuations of the edge and bulk oscillators, which signifies the presence/absence of the TSS. If the inhomogeneity of the natural frequencies is large and/or the linear coupling is weak, we obtain a fully desynchronized state. We note that the parameter where the TSS disappears corresponds to the point at which the dispersion relation of the Hamiltonian becomes gapless due to strong disorders and thus can change its topology. Therefore, the result in Fig. 2 supports the argument that TSS is topologically protected. We can also analyze the robustness of TSS by constructing a one-dimensional model imitating the dynamics of the synchronized edge oscillators in our model (see Supplementary Information).

Here, we emphasize that the TSS is defined as the coexistence of synchronized edge oscillators and desynchronized bulk oscillators with a topological origin. If we set α negative in our model (Eq. (1)), we can damp the bulk oscillations (see Supplementary Information), while the edge ones still exhibit synchronized oscillations (note that a similar synchronized state is observed in previous research [43]). However, such synchronization is not a TSS defined here because the bulk oscillators do not exhibit (chaotic) self-oscillations. Using another Hamiltonian as linear couplings, we can also realize cluster synchronization where the edge oscillators and bulk ones oscillate at different frequencies (see Supplementary Information), which is also out of the range of the TSS.

While we utilize the Hamiltonian featuring exceptional edge modes in Fig. 1, we can also realize TSS by using a Hamiltonian of topological edge modes protected by conventional bulk topology. To demonstrate this, we consider another non-Hermitian Hamiltonian exhibiting lasing edge modes (see Supplementary Information for the detail). Figure 3a,b shows the frequency distributions of nonlinear oscillators with such topological linear couplings. We can confirm the emergence of the TSS, i.e., the edge oscillators are synchronized while the bulk ones are chaotic (see also Supplementary Information). We can also confirm the amplification of the edge oscillators in Fig. 3c as in Fig. 1e. Furthermore, we also find that nonidenti-

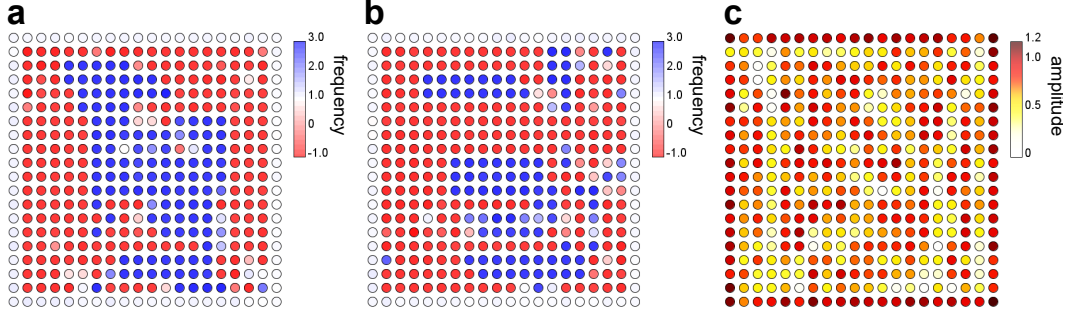


FIG. 3. TSS induced by conventional topological edge modes. **a, b** The frequency of the first component of oscillators at each site is shown. We numerically calculate the dynamics of the model of the TSS (Eq. (1)) with different topological linear couplings from those in Fig. 1, where the edge modes are protected by conventional bulk topology. Panel **a** (**b**) is the snapshot at the time $t = 1000$ ($t = 2000$). Empty sites represent the oscillators oscillating around their natural frequencies. We confirm the coexistence of the synchronized edge oscillators and the desynchronized bulk oscillators. The parameters used are $u = -1$, $u' = 0.02$, $a = 2$, $b = 0.5$, $\alpha = 0.5$, $\beta = 1$, $\omega_0 = 1$, and $\Delta\omega = 0.2$. **c** The panel shows the amplitudes of the oscillators obtained from the numerical simulation of the dynamics of the model considered in panels **a, b**. We check that the amplitudes of most of the edge oscillators are larger than those of the bulk oscillators. The same parameters as panels **a, b** are used in the calculation.

cal oscillators with Hermitian linear couplings can exhibit the TSS (see Supplementary Information). We can obtain such TSS by utilizing non-Hermiticity introduced as the modulated natural amplitudes of nonlinear oscillators and realizing lasing behavior of edge modes. Table I summarizes the properties of our three models. These models indicate that the TSS is ubiquitous in nonlinear oscillators with topological linear couplings exhibiting lasing edge modes.

Chaos in bulk oscillators and the edge-localized Lyapunov vectors.— We next show that the bulk oscillators exhibit chaotic dynamics. In this section, we analyze the chaotic behavior of our first model in Fig. 1 (see Supplementary Information for the results on the other models). Chaos is characterized by the extreme sensitivity to initial conditions, i.e., exponential growth of the initial difference between trajectories. The infinitesimal rate of such exponential divergence is called the Lyapunov exponent [22], and its positivity gives a defining feature of chaos. We numerically calculate the Lyapunov exponents of the first model. Figure 4a shows the obtained ones and the existence of positive Lyapunov exponents indicating the chaos. Lyapunov exponents also tell us the effective degree of freedom of chaotic attractor, Lyapunov dimension defined as $D_L = \sum_{i \leq M} \lambda_i / |\lambda_{M+1}| + M$, where λ_i represents Lyapunov exponents arranged in descending order, and M is the smallest integer that satisfies $\sum_{i \leq M+1} \lambda_i < 0$. Previous studies [28, 29] have revealed that the Lyapunov dimension corresponds to the number of the desynchronized oscillators in the chimera state. In our first model, we obtain the Lyapunov dimension $D_L = 254.568$, which is almost 90 percent of the total degree of freedom of oscillators except for the first and second oscillators from the edge, $D_{\text{bulk}} = 288$. Our Lyapunov analysis thus clearly indicates that the bulk oscillators are desynchronized and exhibit chaotic dynamics. We note that Stuart-Landau oscillators can exhibit two types of chaos, namely, amplitude chaos and phase chaos [44]. In this model, we can see amplitude-chaotic behaviors, e.g., phase slips via

zero amplitude (see Supplementary Information).

Lyapunov vectors can be used to know the local geometric information of chaotic attractors [24]. Specifically, perturbation parallel to a Lyapunov vector is amplified or attenuated in a forward and backward process expressed as $|\delta \vec{Z}(\pm t)| \sim |\delta \vec{Z}(0)| e^{\pm \lambda_i t}$, where λ_i is the associated Lyapunov exponent. In our first model, we reveal that the Lyapunov vectors corresponding to the small Lyapunov exponents are localized at the edge of the system, thus realizing topological edge modes in nonlinear systems. To clearly show such localization to the edge, we define the following index of the proportion of amplitude of the edge oscillators,

$$P_{\text{edge}} = \sum_{i \in \text{edge}} |v_i|^2, \quad (2)$$

where v_i is the i th component of the Lyapunov vector and we sum the squares of the components corresponding to the edge oscillators. This index takes a large value when a Lyapunov vector is localized furthestmost to the edge. Figure 4b shows the proportions of the edge oscillators of the Lyapunov vectors in our first model. One can see the steep increase in the index, which indicates that the first about 80 percent of Lyapunov vectors are extended to the bulk, while the others are localized to the edge. We demonstrate such localization and delocalization of the Lyapunov vectors by plotting them in the real space (see Supplementary Information). It is noteworthy that the Lyapunov exponents decrease around the index where the edge proportions increase. Thus, we expect that perturbation to the edge oscillators is attenuated, which implies stability of their synchronization.

We also evaluate the degree of localization in the entire Lyapunov vectors by calculating inverse participation ratios (IPRs) defined as

$$\text{IPR} = \sum_i |v_i|^4. \quad (3)$$

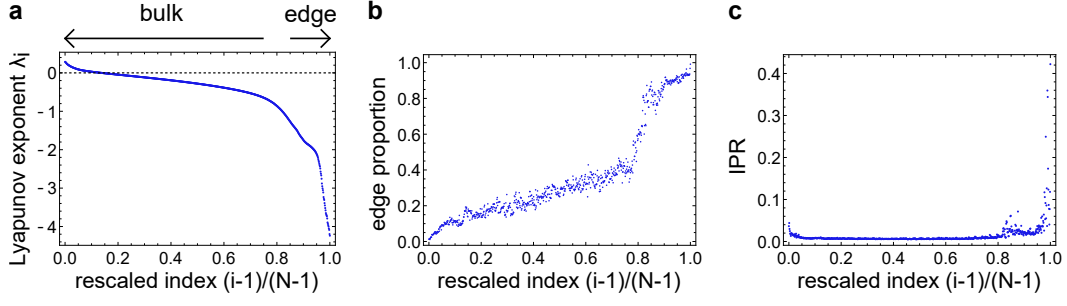


FIG. 4. Lyapunov spectrum and the indices of the localization of the Lyapunov vectors. **a** Lyapunov exponents are calculated from the first model of the TSS (cf. Eq. (1) and Fig. 1). They are arranged in descending order. The index of the Lyapunov exponent is rescaled for the maximum to be unity. The dashed horizontal line corresponds to zero Lyapunov exponents. Some of the Lyapunov exponents are positive, i.e., placed above the dashed line, which indicates the chaotic behavior of the oscillators. The parameters used are $u = -1$, $b = 0.5$, $\alpha = 0.5$, $\beta = 1$, $\omega_0 = 0.2$, and $\Delta\omega = 0.2$. **b** The proportions of the edge amplitudes P_{edge} of the Lyapunov vectors in the TSS are shown. We set the relative index of the Lyapunov vector to be the same as panel **a**. The edge proportions rise steeply around the relative index 0.8. Therefore, the Lyapunov vectors of the small indices spread in the bulk, while those of the large indices are localized at the edge of the system. This increase accompanies the decrease of the Lyapunov exponents in panel **a**, which indicates that the edge localized Lyapunov vectors are dissipative modes. **c** Inverse participation ratios (IPRs) of the Lyapunov vectors are presented. We set the relative index of the Lyapunov vector to be the same as in panel **a**. The IPRs show a small rise around the relative index 0.8, corresponding to the edge localization of the Lyapunov vectors. The IPRs also increase steeply at a larger relative index, which indicates that a few Lyapunov vectors are strongly localized at a few edge sites.

The IPR becomes large when a small number of components of a Lyapunov vector exhibit large amplitudes, that is, it is localized at only a few sites. Figure 4c shows the IPR of the Lyapunov vectors obtained in our first model. There is a slight increase in the IPR around the relative index of the Lyapunov vectors 0.8 as a result of the localization to the edge. The smallness of the increase in the IPR indicates that most of the edge-localized Lyapunov vectors spread at many edge sites, which is reminiscent of conventional topological edge modes in linear systems. We can find another region where the IPR steeply increases. Those large IPRs imply the strong localization of the Lyapunov vectors to a few edge sites. We note that the Lyapunov exponents also decrease in this region, indicating the strong damping of the perturbation corresponding to these localized Lyapunov vectors. While the proportions of the edge oscillators (Eq. (2)) reveal the existence of the edge-localized Lyapunov vectors, IPRs allow us to classify such edge-localized Lyapunov vectors into two groups, the extended ones corresponding to conventional edge modes and the strongly localized ones induced by nonlinearity.

The edge-localized Lyapunov vectors and their negative Lyapunov exponents are related to the edge modes of the effective Hamiltonian obtained via the linearization of the equation. We note that if there are no nonlinear terms (i.e., $\beta = 0$ in our model), Lyapunov exponents and vectors are identical to the imaginary parts of the eigenvalues and eigenvectors of the effective Hamiltonian, respectively. It is noteworthy that non-Hermiticity is essential to realize nonzero imaginary parts of eigenvalues, and nonlinear oscillators ubiquitously exhibit such dissipative and injective effects. In nonlinear systems, we can obtain the effective Hamiltonian by linearizing the equation around the state at each moment. The linear equation governed by the sequence of such effective Hamiltonians describes the time evolution of the difference between the per-

turbed trajectory and the original one. We numerically check that the effective Hamiltonian of our first model exhibits edge modes with negative imaginary parts of the eigenvalues (see Supplementary Information), which indicates the (short-term) stability of the synchronization of the edge oscillators. We note that nonlinear terms lead to a random on-site loss in the effective Hamiltonian. However, topological modes are robust against such disorders and thus still appear from the present effective Hamiltonian.

Emergence of extra topological modes by nonlinearity-induced boundary.— We find that nonlinearity can induce unconventional extra edge modes, which should be the origin of the synchronization of the second oscillators from the edge as discussed in the previous section. Namely, nonlinear systems exhibiting self-excited vibration, including our model, can generate effective boundaries and extra topological modes regardless of the initial conditions. Previous studies [21, 45] have discussed that one can create effective boundaries by externally preparing a localized initial state, whereas effective boundaries in our model analyzed in Fig. 1 spontaneously appear by utilizing the lasing edge modes. To show the existence of such extra boundary modes, we rewrite the equation of our model (Eq. (1)) as $\dot{Z}_j(\mathbf{x}) = -i \sum_k \tilde{H}_{jk}(\mathbf{Z}; \mathbf{x}, \mathbf{x}') Z_k(\mathbf{x}')$, where $\tilde{H}_{jk}(\mathbf{Z}; \mathbf{x}, \mathbf{x}') = H_{jk}(\mathbf{x}, \mathbf{x}') + (-\omega_j(\mathbf{x}) + i\alpha - i\beta|Z_j(\mathbf{x})|^2)\delta_{jk}\delta_{\mathbf{x},\mathbf{x}'}$ represents the state-dependent Hamiltonian which governs the time evolution at each moment. This state-dependent Hamiltonian includes an on-site loss at edge sites, because lasing edge modes of the original Hamiltonian H of our first model amplify the edge oscillators as shown in Fig. 1e. We note that recent research [38] has shown that on-site loss creates an effective boundary, and topological boundary modes can appear at the boundary between the regions with gain and loss. While the previous study has focused on linear dynamics with an externally introduced boundary, in

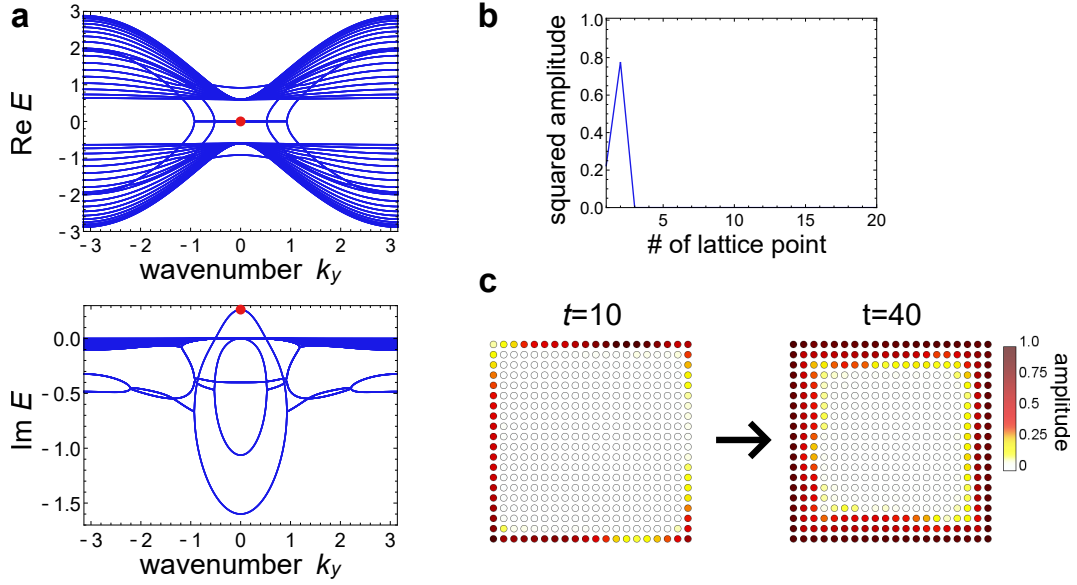


FIG. 5. Dispersion relations and the dynamics demonstrating a spontaneous nonlinearity-induced boundary. **a** We calculate the edge dispersions of the Hamiltonian \tilde{H} of topological insulator laser utilized in our first model under the existence of edge-localized on-site loss. We impose the open (periodic) boundary condition in the x (y) direction. The edge-localized on-site loss corresponds to the effect of nonlinear terms in the case that the edge modes of the original Hamiltonian H are amplified. We find the extra number of gapless modes. Those extra topological modes appear due to the effective boundary created by the nonlinearity-induced edge-localized loss. The parameters used are $u = -1$, $b = 0.8$, $\alpha = 0$, $\beta = 1$, $\omega_0 = 0$, and $\Delta\omega = 0$. **b** The density distribution of one of the extra topological modes (corresponding to the red point in panel **a**) is shown. One can see that this eigenstate exhibits the largest amplitude at the second site, which implies that it is localized at the effective boundary emerging between the first and second sites. **c** We numerically demonstrate the dynamical formation of the extra topological boundary modes. We set the coefficient of the nonlinear term much smaller than that of the linear coupling. The snapshots at the time $t = 10$ ($t = 40$) are shown in the left (right) figure. When the edge oscillators are not fully amplified (corresponding to $t = 10$), the edge-localized loss is not large enough to create an effective boundary. After the edge oscillators are fully amplified, the inside oscillators begin to largely oscillate, which implies the appearance of the extra topological boundary modes.

our model the on-site loss is an emergent feature in the sense that it is spontaneously induced by the nonlinearity.

To explicitly demonstrate the presence of such extra boundary modes, we numerically diagonalize the state-dependent Hamiltonian \tilde{H} with edge-localized loss. Here, we consider the on-site loss that should be induced by lasing edge modes of the original Hamiltonian H used in Fig. 1. Figure 5a shows the dispersion relation of this state-dependent Hamiltonian. We obtain eight gapless modes, which are the twice number of gapless modes compared to the original Hamiltonian without on-site loss (see Supplementary Information for the dispersion relation of the original Hamiltonian). We find positive imaginary parts of eigenvalues and the localization to the second site of the corresponding eigenvectors, which leads to the amplification of the second oscillators from the edge.

We also directly confirm the emergence of the extra boundary modes from the numerical simulation. We set the coefficient of nonlinear terms to be small compared to those of linear coupling H . Figure 5c presents the snapshots of the relative amplitude of each site obtained from the simulation. In the beginning, only the outermost oscillators have large amplitudes, while after a sufficiently long time the inner ones also begin to oscillate with large amplitudes. This behavior represents the emergence of the extra boundary modes after the nonlinearity-

induced loss grows enough to balance with the linear coupling and create an effective boundary.

The presence of the extra boundary modes above can alter the number of the synchronized oscillators in the TSS. Edge-localized on-site loss also exists in the effective Hamiltonian obtained from the linearization of the equation around the state at each moment. Therefore, the number of topological modes can increase in such an effective Hamiltonian via the same mechanism as in the state-dependent Hamiltonian. We confirm the existence of the extra boundary modes and negativity of the imaginary parts of their eigenvalues (see Supplementary Information), which leads to the increase in the number of dissipative Lyapunov vectors.

Applications of TSS.— Damped bulk oscillators in the TSS will create an effective edge, along which the oscillators can be newly synchronized. We here propose several applications of such emerging synchronized oscillators, e.g., on-demand synchronization pattern designing and defect detection.

First, by placing damped oscillators into the bulk, one can arrange synchronized oscillators in an arbitrary pattern. We demonstrate such flexible pattern designing in Fig. 6 (see Supplementary Information for the numerical method to introduce damped oscillators). In Fig. 6b, we define the indicator of the local order parameter as

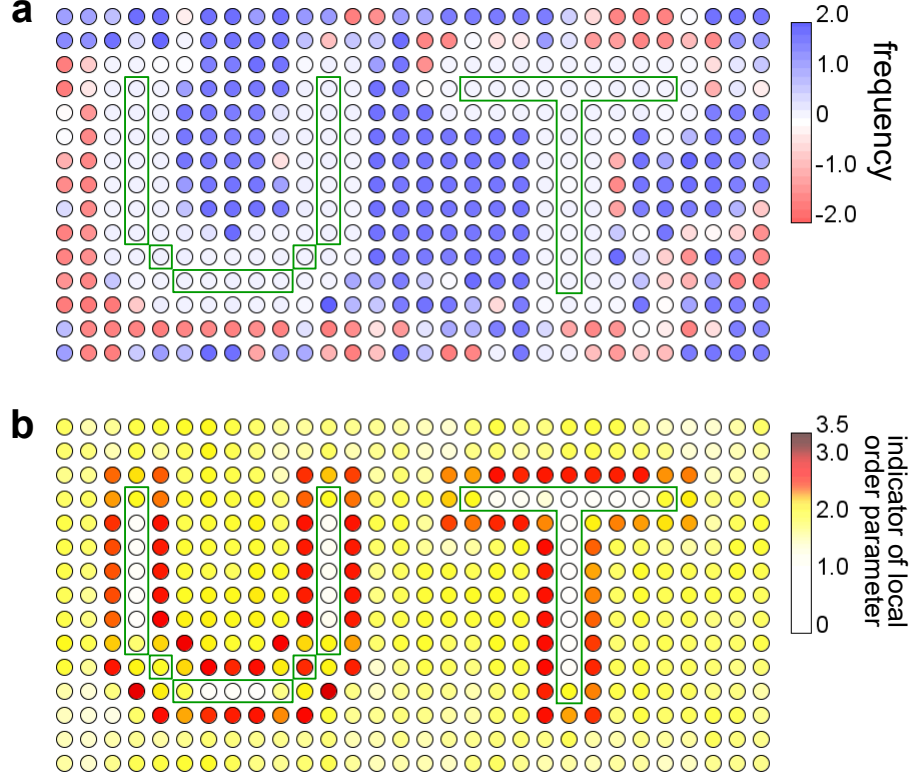


FIG. 6. On-demand pattern designing of the synchronized oscillators. **a,b** We numerically demonstrate that the on-demand pattern designing of the synchronized oscillators is possible by utilizing the TSS. To arrange the synchronized oscillators in the shape of characters, UT, we damp the oscillators encircled by the green boxes and numerically calculate the dynamics of the first model of topological synchronization (cf. Eq. (1) and Fig. 1) under the periodic boundary condition. The parameters used are $u = -1$, $b = 0.3$, $\alpha = 0.5$, $\alpha_d = -100$, $\beta = 1$, $\omega_0 = 0.1$, and $\Delta\omega = 0.2$. **a** The frequencies of the oscillators are shown. The oscillators around the damped ones exhibit a homogeneous frequency, indicating the synchronization of those oscillators. We obtain the desired shape of the collection of the synchronized oscillators. **b** The indicator of the local order parameter $M(x, y)$ (Eq. (4)) at each site is shown. We also confirm the appearance of the desired synchronization pattern from this result.

$$M(x, y; t) = \frac{1}{4T} \int_{t-T}^t dt' \sum_{k=1}^4 |Z_k(x, y) + Z_k(x+1, y) + Z_k(x-1, y) + Z_k(x, y+1) + Z_k(x, y-1)|, \quad (4)$$

which becomes large when the phase of the oscillator matches those of the nearest neighbors. The oscillators around damped ones exhibit the homogeneous frequencies and the large values of the indicator M , thus being synchronized. We note that the synchronization pattern disappears in a topologically trivial system (see Supplementary Information), demonstrating the crucial role played by the topology of the linear coupling.

If some of the oscillators suddenly stop their self-oscillations, the oscillators around them begin to synchronize. Thus, by observing the appearance of a synchronized cluster, we can continuously monitor the formation of the broken oscillators, i.e., defects. To demonstrate such possibility of defect detection using the TSS, we numerically calculate the dynamics of our first model and damp some oscillators in the

middle of the simulation. Figure 7c shows the spatial distribution of the indicator $M(x, y)$ (Eq. (4)) in the steady-state regime. We find the synchronized oscillators that precisely lie along the edges of the defects. In contrast, when the sensors that detect the state of oscillators get broken and are unable to send signals to the central computing system (see Fig. 7b), our method obtains no enhanced signals indicating synchronization. Therefore, we can affirm the existence of broken oscillators from the large value of the indicator $M(x, y)$ (Eq. (4)) even under the nonnegligible possibility of this kind of breakdown of sensors. We numerically check the absence of the signal of synchronization in the case of sensors' disorder (see Fig. 7d).

Meanwhile, a system similar to our model can be realized

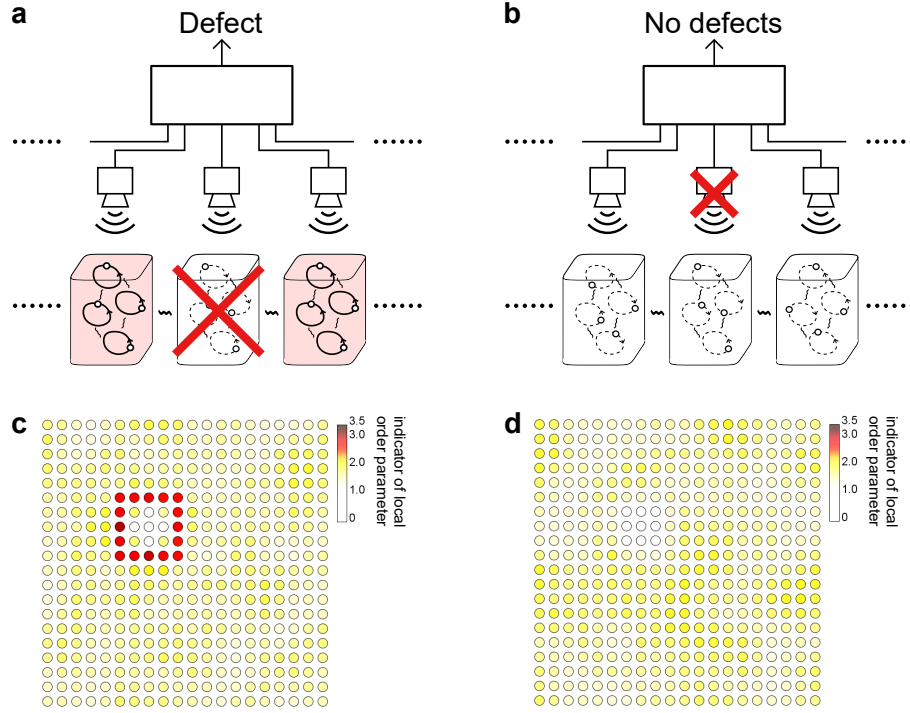


FIG. 7. Applications of the TSS to the defect detection. **a, b** We assume that the dynamics of nonlinear oscillators are detected by sensors. Information of the oscillators' state from the sensors is processed to judge the synchronization of oscillators and the existence of defects. **a** If oscillators are broken and stop their self-oscillation, the oscillators around them are synchronized. By observing such synchronization, we can detect the breakdown of oscillators. **b** When sensors are disordered and send no signals, the oscillators remain desynchronized. Therefore, this kind of breakdown of sensors is distinguishable from the breakdown of oscillators. **c** The indicator of the local order parameter $M(x, y)$ (Eq. (4)) at each site is shown under the existence of the broken oscillators. Large values of the indicator show the synchronization of the oscillators at the corresponding site. One can judge that the oscillators surrounded by synchronized ones are broken. The parameters used are $u = -1$, $b = 0.5$, $\alpha = 0.5$, $\alpha_d = -100$, $\beta = 1$, $\omega_0 = 0.1$, and $\Delta\omega = 0.2$. **d** The indicator $M(x, y)$ at each site is shown under the existence of the broken sensors. The indices are small everywhere, which shows that there are no synchronized oscillators, and thus no oscillators are broken. The parameters used are the same as panel c.

by using an electrical circuit, which is shown in Fig. 8 as a schematic. Using nonlinear resistors, we propose to use van der Pol circuits [46, 47] that simulate nonlinear oscillators. We also utilize negative impedance converters with current inversion [48] to omit the frequency dependence. The dynamics of voltages in this electrical circuit imitates our first model, while the dynamics of van der Pol circuits is different from the Stuart-Landau oscillators (see Supplementary Information for the derivation of circuit equations). We note that one can realize the TSS without fine-tuning of the circuit constant of each element due to the topological protection of the TSS (see Supplementary Information). Our model should also be relevant to broad ranges of other physical systems. Especially, we expect that it is possible to realize the TSS in photonic systems, where topology [20, 21, 39], non-Hermiticity [38, 49, 50], and nonlinearity [3, 4] can be intertwined.

Summary and discussions.— We proposed a robust mechanism to control synchronization, namely, topological synchronization where edge oscillators synchronize while bulk ones exhibit chaotic dynamics. We termed such coexistence state of chaotic bulk motions and synchronized edge oscillators as the topological synchronized state (TSS) and analyzed the lo-

calized behaviors of its models. The edge modes of the topological linear couplings between oscillators are represented by the Lyapunov vectors localized at the edge of the system. The mechanism relies on topology in the wavenumber space and thus is different from the conventional mechanism of chimera states; the latter can be explained from the self-consistency analysis and spatial variation of local order parameters [25, 26]. We also demonstrated that nonlinearity induces emerging effective boundaries, which leads to extra topological modes unique to nonlinear systems. As examples of applications, we showed that one can realize arbitrary patterns of synchronized oscillators by using topological synchronization. We also revealed that chaotic nonlinear systems can be used to detect disordered oscillators. Our model can be realized by utilizing an electrical circuit. Our proposal provides a general method to robustly and geometrically control the nonlinear oscillators by combining nonlinearity and topology.

It is noteworthy that the TSS should ubiquitously appear in nonlinear systems with a topological effective Hamiltonian. In this paper, we confirmed the emergence of TSS in homogeneous Stuart-Landau oscillators whose linear couplings are described by Hamiltonians of two types of lasing edge

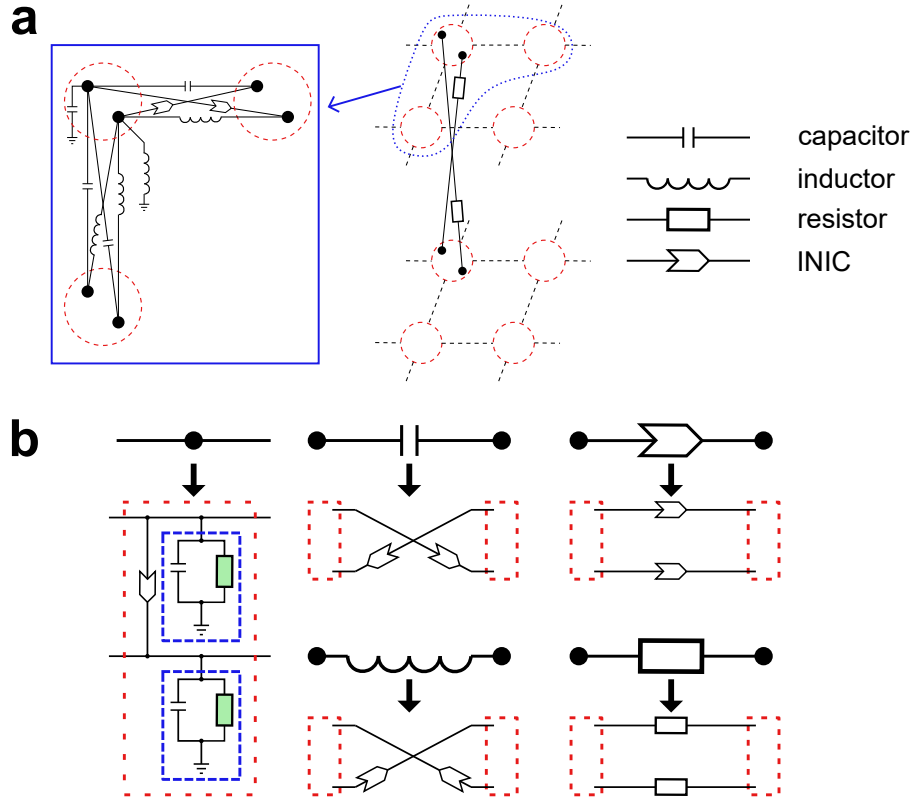


FIG. 8. Proposed electrical circuit to realize topological synchronization. **a** A linear system described by the effective Hamiltonian of topological insulator laser can be constructed by an electrical circuit using capacitors, inductors, resistors, and negative impedance converters with current inversion (INICs). We consider two layers of square lattices, and each lattice point (a red dashed circle) has two sites (black dots). The dynamics of the voltages at the sites follows the Hamiltonian of topological insulator laser (Supplementary Eq. (S1)). The left inset represents the detail of the circuit in each layer (corresponding to the enlarged view of the sites encircled by the blue dot curve in the middle panel). The middle panel shows how to connect the sites of the different layers. The legend shows the correspondence of the figures and the circuit elements. **b** We can construct the model of the TSS by replacing the circuit elements in panel **a**. We substitute each site (a black dot) into two van-del-Pol circuits (blue dashed squares) coupled by an INIC. Green-filled boxes represent the nonlinear resistors. The other panels represent the substitution rules of capacitors, inductors, resistors, and INICs. We only use resistors and INICs to avoid frequency dependence of impedance. Red dashed squares represent the coupled van der Pol circuits in the left panel.

modes protected by different topological mechanisms. We also discussed the TSS utilizing a Hermitian topological linear coupling and inhomogeneity of oscillators (cf. Table I). Furthermore, there is no need to judiciously adjust the parameters as discussed in Supplementary Information, which should be of practical advantage to realize the TSS in a variety of systems. Despite the broadness of models considered in this work, the TSS in identical oscillators induced by a Hermitian topological Hamiltonian still remains an intriguing problem. This may be possible by utilizing nonlinearity-induced non-Hermitian effect and realizing positive imaginary parts only in bulk modes of the effective Hamiltonian obtained by linearization of the equation (cf. Supplementary Information). Furthermore, we anticipate that other nonlinear oscillators than the Stuart-Landau model (e.g., the Fitzhugh-Nagumo model [51, 52]) can exhibit the TSS, because topological edge modes should be stable against the change of the on-site loss induced by the nonlinear terms.

We thank Eiji Saitoh and Shin-ichi Sasa for valuable discus-

sions. K.S. is supported by World-leading Innovative Graduate Study Program for Materials Research, Industry, and Technology (MERIT-WINGS) of the University of Tokyo. K.S. is also supported by JSPS KAKENHI Grant Number JP21J20199. Y.A. is supported by JSPS KAKENHI Grant Number JP19K23424. T.S. is supported by JSPS KAKENHI Grant Numbers JP16H02211 and JP19H05796. T.S. is also supported by Institute of AI and Beyond of the University of Tokyo.

* sone@noneq.t.u-tokyo.ac.jp

- [1] Buck, J. Synchronous rhythmic flashing of fireflies. II. *Quart. Rev. Biol.* **63**, 265–289 (1988).
- [2] Luo, C. H., & Rudy, Y. A model of the ventricular cardiac action potential. Depolarization, repolarization, and their interaction. *Circ. Res.* **68**, 1501–1526 (1991).
- [3] Kozyreff, G., Vladimirov, A. G., & Mandel, P. Global Coupling

- with Time Delay in an Array of Semiconductor Lasers. *Phys. Rev. Lett.* **85**, 3809–3812 (2000).
- [4] Ludwig, M. & Marquardt, F. Quantum Many-Body Dynamics in Optomechanical Arrays. *Phys. Rev. Lett.* **111**, 073603 (2013).
- [5] Blaabjerg, F., Teodorescu, R., Liserre, M., & Timbus, A. V. Overview of Control and Grid Synchronization for Distributed Power Generation Systems. *IEEE Trans. Ind. Electron.* **53**, 1398–1409 (2006).
- [6] Wiesenfeld, K., Colet, P., & Strogatz, S. H. Synchronization Transitions in a Disordered Josephson Series Array. *Phys. Rev. Lett.* **76**, 404–407 (1996).
- [7] Acebrón, J. A., Bonilla, L. L., Pérez, V. C. J., Ritort, F., & Spigler, R. The Kuramoto model: A simple paradigm for synchronization phenomena. *Rev. Mod. Phys.* **77**, 137–185 (2005).
- [8] Dibner, C., Schibler, U., & Albrecht, U. The Mammalian Circadian Timing System: Organization and Coordination of Central and Peripheral Clocks. *Annu. Rev. Physiol.* **72**, 517–549 (2010).
- [9] Lee, T. E. & Sadeghpour, H. R. Quantum Synchronization of Quantum van der Pol Oscillators with Trapped Ions. *Phys. Rev. Lett.* **111**, 234101 (2013).
- [10] Laskar, A. W. et al., Observation of Quantum Phase Synchronization in Spin-1 Atoms. *Phys. Rev. Lett.* **125**, 013601 (2020).
- [11] Sieber, J., Omel'chenko, O. E., & Wolfrum, M. Controlling Unstable Chaos: Stabilizing Chimera States by Feedback. *Phys. Rev. Lett.* **112**, 054102 (2014).
- [12] Isele, T., Hizanidis, J., Provata, A., & Hövel, P. Controlling chimera states: The influence of excitable units. *Phys. Rev. E* **93**, 022217 (2016).
- [13] Zhang, Y., Nicolaou, Z. G., Hart, J. D., Roy, R., & Motter, A. E. Critical Switching in Globally Attractive Chimeras. *Phys. Rev. X* **10**, 011044 (2020).
- [14] Kane, C. L. & Mele, E. J. Z_2 Topological Order and the Quantum Spin Hall Effect. *Phys. Rev. Lett.* **95**, 146802 (2005).
- [15] Qi, X. L. & Zhang, S. C. Topological insulators and superconductors. *Rev. Mod. Phys.* **83**, 1057–1110 (2011).
- [16] Smirnova, D., Leykam, D., Chong, Y., & Kivshar, Y. Nonlinear topological photonics. *Appl. Phys. Rev.* **7**, 021306 (2020).
- [17] Ota, Y. et al., Active topological photonics. *Nanophotonics* **9**, 547–567 (2020).
- [18] Zhang, Z. et al., Observation of edge solitons in photonic graphene. *Nat. Commun.* **11**, 1902 (2020).
- [19] Chen, B. G., Upadhyaya, N., & Vitelli, V. Nonlinear conduction via solitons in a topological mechanical insulator. *Proc. Natl. Acad. Sci. USA* **111**, 13004–13009 (2014).
- [20] Leykam, D. & Chong, Y. D. Edge Solitons in Nonlinear-Photonic Topological Insulators. *Phys. Rev. Lett.* **117**, 143901 (2016).
- [21] Lumer, Y., Plotnik, Y., Rechtsman, M. C., & Segev, M. Self-Localized States in Photonic Topological Insulators. *Phys. Rev. Lett.* **111**, 243905 (2013).
- [22] Oseledets, V. A multiplicative ergodic theorem. Characteristic Ljapunov, exponents of dynamical systems. *Trans. Moscow. Math. Soc.* **19**, 197–231 (1968).
- [23] Takeuchi, K. A., Ginelli, F., & Chaté, H. Lyapunov Analysis Captures the Collective Dynamics of Large Chaotic Systems. *Phys. Rev. Lett.* **103**, 154103 (2009).
- [24] Ginelli, F., Chaté, H., Livi, R., & Politi, A. Covariant Lyapunov vectors. *J. Phys. A* **46**, 254005 (2013).
- [25] Kuramoto, Y. & Battogtokh, D. Coexistence of Coherence and Incoherence in Nonlocally Coupled Phase Oscillators. *Nonlinear Phenom. Complex. Syst.* **5**, 380 (2002).
- [26] Abrams, D. M. & Strogatz, S. H. Chimera States for Coupled Oscillators. *Phys. Rev. Lett.* **93**, 174102 (2004).
- [27] Panaggio, M. J. & Abrams, D. M. Chimera states: coexistence of coherence and incoherence in networks of coupled oscillators. *Nonlinearity* **28**, R67–R87 (2015).
- [28] Wolfrum, M., Omel'chenko, O. E., Yanchuk, S., & Maistrenko, Y. L. Spectral properties of chimera states. *Chaos* **21**, 013112 (2011).
- [29] Höhlein, K., Kemeth, F. P., & Krischer, K. Lyapunov spectra and collective modes of chimera states in globally coupled Stuart-Landau oscillators. *Phys. Rev. E* **100**, 022217 (2019).
- [30] Majhi, S., Bera, B. K., Ghosh, D., & Perc, M. Chimera states in neuronal networks: A review. *Phys. Life Rev.* **28**, 100–121 (2019).
- [31] Tinsley, M. R., Nkomo, S., & Showalter, K. Chimera and phase-cluster states in populations of coupled chemical oscillators. *Nat. Phys.* **8**, 662–665 (2012).
- [32] Martens, E. A., Thutupalli, S., Fourrière, A., & Hallatschek, O. Chimera states in mechanical oscillator networks. *Proc. Natl. Acad. Sci. USA* **110**, 10563–10567 (2013).
- [33] Gong, Z. et al., Topological Phases of Non-Hermitian Systems. *Phys. Rev. X* **8**, 031079 (2018).
- [34] Shen, H., Zhen, B., & Fu, L. Topological Band Theory for Non-Hermitian Hamiltonians. *Phys. Rev. Lett.* **120**, 146402 (2018).
- [35] Kunst, F. K., Edvardsson, E., Budich, J. C., & Bergholtz, E. J. Biorthogonal Bulk-Boundary Correspondence in Non-Hermitian Systems. *Phys. Rev. Lett.* **121**, 026808 (2018).
- [36] Yao, S. & Wang, Z. Edge States and Topological Invariants of Non-Hermitian Systems. *Phys. Rev. Lett.* **121**, 086803 (2018).
- [37] Fruchart, M., Hanai, R., Littlewood, P. B., & Vitelli, V. Non-reciprocal phase transitions. *Nature* **592**, 363–369 (2021).
- [38] Zhao, H. et al., Non-Hermitian topological light steering. *Science* **365**, 1163–1166 (2019).
- [39] Harari, G. et al., Topological insulator laser: Theory. *Science* **359**, 1230 (2018).
- [40] Song, A. Y. et al., \mathcal{PT} -Symmetric Topological Edge-Gain Effect. *Phys. Rev. Lett.* **125**, 033603 (2020).
- [41] Sone, K., Ashida, Y., & Sagawa, T. Exceptional non-Hermitian topological edge mode and its application to active matter. *Nat. Commun.* **11**, 5745 (2020).
- [42] Stuart, J. On the non-linear mechanics of wave disturbances in stable and unstable parallel flows Part 1. The basic behaviour in plane Poiseuille flow. *J. Fluid Mech.* **9**, 353–370 (1960).
- [43] Wächter, C. W., Bastidas, V. M., Schaller, G., & Munro, W. J. Dissipative nonequilibrium synchronization of topological edge states via self-oscillation. *Phys. Rev. B* **102**, 014309 (2020).
- [44] Shraiman, B. I. et al., Spatiotemporal chaos in the one-dimensional complex Ginzburg-Landau equation. *Physica D* **57**, 241–248 (1992).
- [45] Tuloup, T., Bomantara, R. W., Lee, C. H., & Gong, J. Nonlinearity induced topological physics in momentum space and real space. *Phys. Rev. B* **102**, 115411 (2020).
- [46] Van der Pol, B. On "relaxation-oscillations" *Philos. Mag.* **2**, 978 (1926).
- [47] Johnson, B. B., Dhople, S. V., and Hamadeh, A. O., & Krein, P. T. Synchronization of Parallel Single-Phase Inverters With Virtual Oscillator Control. *IEEE Trans. Circuits Syst. I Regul. Pap.* **61**, 834–844 (2014).
- [48] Hofmann, T., Helbig, T., Lee, C. H., Greiter, M., & Thomale, R. Chiral Voltage Propagation and Calibration in a Topoelectrical Chern Circuit. *Phys. Rev. Lett.* **122**, 247702 (2019).
- [49] El-Ganainy, Makris, R., K. G., Christodoulides, D. N., & Musslimani, Z. H. Theory of coupled optical PT-symmetric structures. *Opt. Lett.* **32**, 2632–2634 (2007).
- [50] Xu, H., Mason, D., Jiang, L., & Harris, J. G. E. Topological energy transfer in an optomechanical system with exceptional points. *Nature* **537**, 80–83 (2016).

- [51] Fitzhugh, R. Impulses and Physiological States in Theoretical Models of Nerve Membrane. *Biophys. J.* **1**, 445–466 (1961).
- [52] Nagumo, J., Arimoto, S., & Yoshizawa, S. An Active Pulse Transmission Line Simulating Nerve Axon. *Proc. IRE* **50**, 2061–2070 (1962).
-

Supplementary Materials

Hamiltonian of topological lasing modes used as the linear coupling

In this section, we explicitly present the linear couplings used in our two models (cf. Figs. 1, 3). To describe the linear coupling between nonlinear oscillators in our first model (cf. Fig. 1), we utilize the Hamiltonian of topological lasing modes [40, 41]. This Hamiltonian is expressed in the wavenumber space as

$$H(\mathbf{k}) = (u + \cos k_x + \cos k_y)I_2 \otimes \sigma_z + \sin k_y I_2 \otimes \sigma_y + \sin k_x \sigma_z \otimes \sigma_x + ib\sigma_x \otimes \sigma_x \quad (\text{S1})$$

where I_2 is the 2×2 identity matrix and $\sigma_{x,y,z}$ are the Pauli matrices

$$\sigma_x = \begin{pmatrix} 0 & 1 \\ 1 & 0 \end{pmatrix}, \quad \sigma_y = \begin{pmatrix} 0 & -i \\ i & 0 \end{pmatrix}, \quad \sigma_z = \begin{pmatrix} 1 & 0 \\ 0 & -1 \end{pmatrix}. \quad (\text{S2})$$

We can obtain the following real-space description by the inverse Fourier transformation:

$$\begin{aligned} H_{jk}(\mathbf{x}, \mathbf{x}') = & \left(u\delta_{\mathbf{x},\mathbf{x}'} + \frac{\delta_{\mathbf{x}+\mathbf{e}_x,\mathbf{x}'} + \delta_{\mathbf{x}-\mathbf{e}_x,\mathbf{x}'} + \delta_{\mathbf{x}+\mathbf{e}_y,\mathbf{x}'} + \delta_{\mathbf{x}-\mathbf{e}_y,\mathbf{x}'}}{2} \right) (I_2 \otimes \sigma_z)_{jk} + i \frac{\delta_{\mathbf{x}+\mathbf{e}_y,\mathbf{x}'} - \delta_{\mathbf{x}-\mathbf{e}_y,\mathbf{x}'}}{2} (I_2 \otimes \sigma_y)_{jk} \\ & + i \frac{\delta_{\mathbf{x}+\mathbf{e}_x,\mathbf{x}'} - \delta_{\mathbf{x}-\mathbf{e}_x,\mathbf{x}'}}{2} (\sigma_z \otimes \sigma_x)_{jk} + ib\delta_{\mathbf{x},\mathbf{x}'} (\sigma_x \otimes \sigma_x)_{jk}, \end{aligned} \quad (\text{S3})$$

where $\delta_{\mathbf{x},\mathbf{x}'}$ represents the Kronecker delta and $\mathbf{e}_{x,y}$ are the lattice vectors in the x or y direction. In our first model, we introduce linear couplings corresponding to this real-space description of the Hamiltonian. This Hamiltonian is constructed from the Qi-Wu-Zhang (QWZ) model [53], which is a model of the Chern insulator. In more detail, we combine the QWZ model H_{QWZ} and its time-reversal counterpart H_{QWZ}^* by the non-Hermitian coupling $ib\sigma_x \otimes \sigma_x$.

In Fig. 3, we consider another Hamiltonian to describe the linear couplings, where the lasing edge modes are protected by conventional bulk topology. The Hamiltonian is described in the real space as

$$\begin{aligned} H_{jk}(\mathbf{x}, \mathbf{x}') = & \left(u\delta_{\mathbf{x},\mathbf{x}'} + \frac{\delta_{\mathbf{x}+\mathbf{e}_x,\mathbf{x}'} + \delta_{\mathbf{x}-\mathbf{e}_x,\mathbf{x}'} + \delta_{\mathbf{x}+\mathbf{e}_y,\mathbf{x}'} + \delta_{\mathbf{x}-\mathbf{e}_y,\mathbf{x}'}}{2} \right) \left[\frac{a+1}{2} (I_2 \otimes \sigma_z)_{jk} + \frac{a-1}{2} (\sigma_z \otimes \sigma_z)_{jk} \right] \\ & + i \frac{\delta_{\mathbf{x}+\mathbf{e}_y,\mathbf{x}'} - \delta_{\mathbf{x}-\mathbf{e}_y,\mathbf{x}'}}{2} \left[\frac{a+1}{2} (I_2 \otimes \sigma_y)_{jk} + \frac{a-1}{2} (\sigma_z \otimes \sigma_y)_{jk} \right] \\ & + i \frac{\delta_{\mathbf{x}+\mathbf{e}_x,\mathbf{x}'} - \delta_{\mathbf{x}-\mathbf{e}_x,\mathbf{x}'}}{2} \left[\frac{a+1}{2} (I_2 \otimes \sigma_x)_{jk} + \frac{a-1}{2} (\sigma_z \otimes \sigma_x)_{jk} \right] \\ & + ib\delta_{\mathbf{x},\mathbf{x}'} (\sigma_x \otimes I_2)_{jk} + iu'\delta_{\mathbf{x},\mathbf{x}'} (\sigma_z \otimes I_2)_{jk}, \end{aligned} \quad (\text{S4})$$

where a, b, u , and u' are real parameters, and $\sigma_i, \delta_{\mathbf{x},\mathbf{x}'}$ represent the i th component of the Pauli matrices and the Kronecker delta. This Hamiltonian is also constructed from two layers of the QWZ model, H_{QWZ} and aH_{QWZ} combined by the non-Hermitian coupling $ib\sigma_x \otimes I_2$.

Detail of the numerical simulation of the model of topological synchronization

We simulate the dynamics of our first model (Eq. (1), Supplementary Eq. (S1)) by using the fourth-order Runge-Kutta method. To calculate the time evolution of the complex-valued state variables, we deal with real and imaginary parts of those variables separately as $Z_i(x, y) = X_i(x, y) + iY_i(x, y)$. Real and imaginary coefficients are substituted as $aZ \rightarrow a(X, Y)^T$ and $ibZ \rightarrow -ib\sigma_y(X, Y)^T$, where a, b are real, and σ_y is the Pauli matrix. We arrange the 20×20 sites which have four complex Stuart-Landau oscillators for each. We impose the open boundary condition both in the x and y direction. We set the natural frequency of each oscillator $\omega_0 + \Omega$ with Ω being a random value from uniform distributions ranging $[-\Delta\omega, \Delta\omega]$. The numerical calculation starts from the random initial condition, where real and imaginary parts of the initial state variables are the random value from uniform distributions ranging $[-0.1, 0.1]$. In Fig. 1, we set the time step $dt = 0.005$ and use the parameters $u = -1$, $b = 0.5$, $\alpha = 0.5$, $\beta = 1$, $\omega_0 = 1$, and $\Delta\omega = 0.2$. In Figs. 1c,d, we demonstrate the frequency distribution. We define the phase of each oscillator as $\text{Im} \log Z_i(x, y)$. We calculate and plot the time-averaged variation of the phase, setting the time window as $T_o = 10$. In Figs. 1c,d, we only plot the frequency of the first component of oscillators at each site. We also plot the amplitude of the first component of oscillators $|Z_1(x, y)|$ in Fig. 1e.

In Fig. 3, we show the dynamics of nonlinear oscillators in the same way as in Fig. 1. The parameters used are $u = -1$, $u' = 0.02$, $a = 2$, $b = 0.5$, $\alpha = 0.5$, $\beta = 1$, $\omega_0 = 1$, and $\Delta\omega = 0.2$. We set the time step $dt = 0.005$. We plot the time-averaged variation of the phase, i.e., the frequency of each oscillator at the first component of the lattice point in Figs. 3a,b. We also plot the amplitude of the first component of oscillators $|Z_1(x, y)|$ in Fig. 3c.

Calculations on the phase diagram

To obtain Fig. 2, we numerically calculate the dynamics of our first model (Eq. (1), Supplementary Eq. (S3)) at different strengths of the linear coupling and inhomogeneity of the natural frequencies. We introduce the parameter of the strength of the linear coupling c by rewriting the equation of our model (Eq. (1)) as

$$\frac{d}{dt}Z_j(\mathbf{x}) = (i\omega_j(\mathbf{x}) + \alpha - \beta|Z_j(\mathbf{x})|^2)Z_j(\mathbf{x}) - ic \sum_{k, \mathbf{x}'} H_{jk}(\mathbf{x}, \mathbf{x}')Z_k(\mathbf{x}'). \quad (\text{S5})$$

We change the parameter c from 0.2 to 2 at intervals of 0.2. We also change the inhomogeneity of the natural frequencies $\Delta\omega$ from 0 to 2 at intervals of 0.1. We fix the other parameters as $u = -1$, $b = 0.5$, $\alpha = 0.5$, $\beta = 1$, and $\omega_0 = 1$. At each parameter, we calculate the dynamics and frequencies of oscillators in a 20×20 square lattice by using the fourth-order Runge-Kutta method as in Fig. 1. Then, at time $t = 100$, we calculate the standard deviations of the frequencies of the outermost oscillators and the bulk ones whose x and y coordinates satisfy $6 \leq x \leq 15$ and $6 \leq y \leq 15$. We plot the standard deviation of the frequencies of the outermost oscillators divided by that of the bulk ones in Fig. 2.

We also perform the numerical clustering of two-dimensional data composed of the pair of the standard deviations of the frequencies of the edge and bulk oscillators. We utilize the k -means method to conduct such clustering. We set the number of clusters as $k = 2$. We determine the symbol used at each point in Fig. 2 based on which cluster the corresponding two-dimensional data point belongs to.

Numerical methods of Lyapunov exponents and Lyapunov vectors

We calculate the Lyapunov exponents and vectors of our first model (Eq. (1), Supplementary Eq. (S3)) by utilizing the Shimada-Nagashima algorithm [54] and Ginelli's algorithm [55]. In those calculations, we arrange 10×10 sites and impose the open boundary condition. We deal with real and imaginary parts of the state variables separately as in the numerical calculation of our model (see the previous section). We first calculate the dynamics of our first model from the random initial condition as in Fig. 1. Here, we set the time step as $\Delta t = 0.1$. The obtained trajectory is used to determine the infinitesimal rate of change of the difference between the perturbed and original trajectories. We arrow an initialization period of $T_{\text{ini}} = 1000$ to stabilize the dynamics into a chaotic attractor. We repeatedly perform the QR decomposition based on the matrices derived from the linearization of the equation and the obtained trajectory from $t = T_{\text{ini}}$ to $t = T_{\text{ini}} + 20000$. The averages of the logarithmic diagonal entries of the R matrices converge to Lyapunov exponents. To omit the effect of the initial condition, we use the R matrices obtained from the time $t = T_{\text{ini}} + 10000$ to $t = T_{\text{ini}} + 20000$ to calculate the Lyapunov exponents. We also utilize those R matrices to calculate the Lyapunov vectors. We iteratively multiply the inverse of obtained R matrices to a randomly-obtained upper-triangle matrix. Finally, the product of the obtained upper-triangle matrix and the Q matrix obtained in the calculation of the Lyapunov exponents represents the set of the Lyapunov vectors.

Numerical methods of the emergent nonlinearity-induced boundary

To show the emergence of the extra topological boundary modes by the emergent nonlinearity-induced boundary, we diagonalize the state-dependent Hamiltonian $\tilde{H}(\mathbf{Z})$ under the open (periodic) boundary condition in the x (y) direction. We perform the inverse Fourier transformation of the Hamiltonian (Supplementary Eq. (S1)) used in our first model only in the x direction. We divide the real and imaginary parts of the state variables as in the simulation of the dynamics of our model and consider the twice size of the matrix compared to the Hamiltonian (Supplementary Eq. (S1)). We consider the 1×20 supercell structure. To determine the strength of the nonlinear loss terms (i.e., $-\beta|z|^2z$), we first diagonalize the Hamiltonian without nonlinear loss terms. We obtain four edge modes $v_j^i(x)$ ($i = 1, \dots, 4$ is the index of the edge modes and $j = 1, \dots, 4$ represents the component of oscillators at each site) with maximum imaginary parts of eigenvalues $\text{Im } E_0$ at the wavenumber $k = 0$. Then, we introduce the on-site loss $-ia(|v_j^1(x)|^2 + |v_j^2(x)|^2 + |v_j^3(x)|^2 + |v_j^4(x)|^2)Z_j(x)$, where the coefficient is set to be $a = \text{Im } E_0$ to balance gain and loss applied to the edge modes $v_j^i(x)$. Thus, this on-site loss corresponds to the case that the edge modes in

the Hamiltonian without the nonlinearity-induced on-site loss are fully amplified. Finally, we diagonalize the Hamiltonian with this nonlinear on-site loss term at each wavenumber and obtain the dispersion relation in Fig. 5a and the eigenvector of the edge mode in Fig. 5b.

We also calculate the dynamics of the extra boundary modes. As in the calculation of the dynamics in Fig. 1, we use the fourth-order Runge-Kutta method and consider the 20×20 square lattice with the open boundary to simulate the dynamics of nonlinear oscillators with linear couplings described by the Hamiltonian (Supplementary Eq. (S3)). By using the parameters $\alpha = 5 \times 10^{-5}$ and $\beta = 1 \times 10^{-4}$, we realize the situation that the nonlinearity has a negligible effect on the dynamics at the initial stage of the simulation. We consider the random initial condition, where real and imaginary parts of the initial state variables are the random value from uniform distributions ranging $[-0.001, 0.001]$. We set the time step $dt = 0.005$. The other parameters used are $u = -1$, $b = 0.8$, $\omega_0 = 0.1$, and $\Delta\omega = 0.2$.

Numerical methods of the on-demand pattern designing

To demonstrate the possibility of arranging synchronized oscillators in a desired pattern, we calculate the dynamics of our first model (Eq. (1), Supplementary Eq. (S3)) under the existence of damped oscillators (see Fig. 6). We implement damped oscillators by setting $\alpha = -100$ at the corresponding sites. We arrange 15×30 sites and impose the periodic boundary condition both in the x and y direction. As in the numerical simulation of the dynamics of our model, we utilize the fourth-order Runge-Kutta method. We start the calculation from the random initial condition, where real and imaginary parts of the initial state variables are the random value from uniform distributions ranging $[-0.1, 0.1]$. We set the time step $dt = 0.005$ and use the parameters $u = -1$, $b = 0.3$, $\alpha = 0.5$, $\beta = 1$, $\omega_0 = 0.1$, and $\Delta\omega = 0.2$. We calculate the frequency of each oscillator from the time-averaged variation of the phase, setting the time window as $T_o = 20$. We also set the time window to calculate the indicators of local order parameters as $T = 100$.

Numerical methods of the defect detection

In the demonstration of the defect detection by using the TSS (cf. Fig. 7), we calculate the dynamics of our first model (Eq. (1), Supplementary Eq. (S3)) under the periodic boundary condition by the fourth-order Runge-Kutta method. To implement the broken oscillators in Fig. 7c, we change the parameters α at the corresponding sites from 0.5 to -100 at the time $t = 200$. On the other hand, to simulate the disorders of sensors, we assume $Z_i(x, y) = 0$ only in the calculation of the indicator of the local order parameter (Eq. (4)). We consider the random initial condition, where real and imaginary parts of the initial state variables are the random value from uniform distributions ranging $[-0.1, 0.1]$. We set the time step $dt = 0.005$ and use the parameters $u = -1$, $b = 0.5$, $\alpha = 0.5$, $\beta = 1$, $\omega_0 = 1$, and $\Delta\omega = 0.2$. We calculate the frequency of each oscillator from the time-averaged variation of the phase, setting the time window as $T_o = 5$. We also set the time window to calculate the indicators of local order parameters as $T = 100$.

Cluster synchronization in the case of another effective Hamiltonian with topological lasing modes

The topological synchronized state (TSS) needs the instability of bulk oscillators to desynchronize them. On the other hand, we numerically check that even if the linear coupling shows topological lasing edge modes, there is a possibility that bulk oscillators stably synchronize in some models, which indicates the absence of the TSS in such models. Here we consider the following Hamiltonian of topological lasing modes:

$$H(\mathbf{k}) = (u + \cos k_x + \cos k_y)\sigma_z + (\sin k_y + i\gamma \cos k_y)\sigma_y + \sin k_x \sigma_x, \quad (\text{S6})$$

where $\sigma_{x,y,z}$ are the Pauli matrices, and I_2 is the 2×2 identity matrix. This Hamiltonian exhibits lasing modes localized only at the right side of the system. Supplementary Figure S1 shows the band structure calculated under the open (periodic) boundary condition in the x (y) direction, which shows the existence of lasing edge modes. We arrange two Stuart-Landau oscillators (cf. Eq. (1) in the main text) at each site of a 20×20 square lattice and combine them by the linear coupling described by the Hamiltonian (Supplementary Eq. (S6)). We assume the open (periodic) boundary condition in the x (y) direction. By calculating the dynamics of this model as in Fig. 1 in the main text, we find that the bulk and left-side oscillators also synchronize. Supplementary Figure S2 shows the frequency of the oscillator at each site. One can confirm that the bulk and left-side oscillators exhibit a homogeneous frequency that is different from that of the right-side oscillators. Thus, the bulk and left-side oscillators form another synchronized cluster, which indicates the absence of the TSS. We note that similar cluster synchronization is studied in one- and two-dimensional nonlinear topological systems [56].

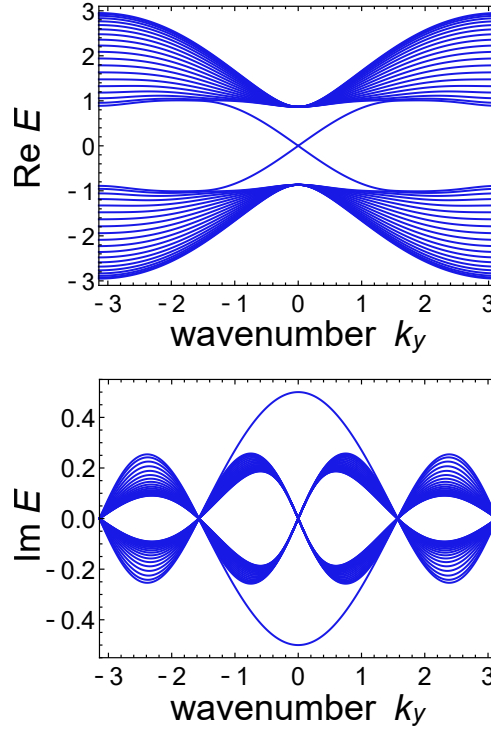


FIG. S1. Dispersion relation of the lasing modes localized at the right edge. We calculate the dispersion relation of the Hamiltonian of topological lasing modes (Supplementary Eq. (S6)). We consider the open (periodic) boundary condition in the x (y) direction and arrange 20 sites in the x direction. We obtain a gapless edge band with positive imaginary parts of eigenvalues. This gapless band corresponds to lasing edge modes localized at the right side. The parameters used are $u = -1$ and $\gamma = 0.5$.

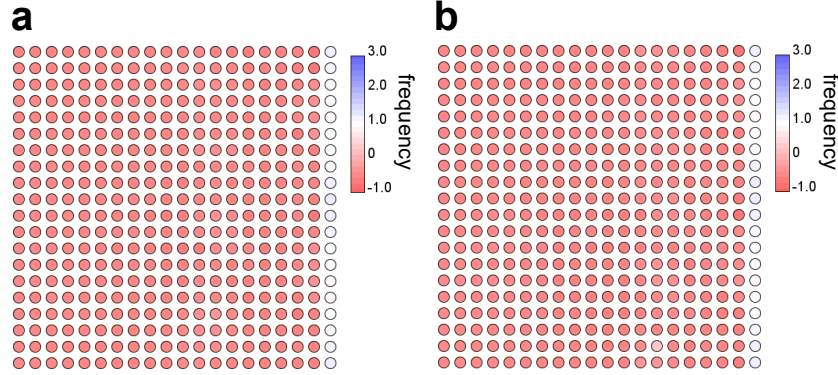


FIG. S2. Cluster synchronization from a topological Hamiltonian. We calculate the dynamics of the Stuart-Landau oscillators with linear coupling described by a Hamiltonian of topological lasing modes that is different from the Hamiltonian considered in the main text (Supplementary Eq. (S6)). Panel **a** (**b**) shows the snapshot of the frequency distribution of the first component of oscillators at the time $t = 1000$ ($t = 2000$). The bulk and left-side oscillators exhibit homogeneous and constant frequency, which is different from that of the right-side oscillators. Therefore, the bulk oscillators form a synchronized cluster, indicating the absence of the topological synchronized state (TSS). The parameters used are $u = -1$, $\gamma = 0.5$, $\alpha = 0.5$, $\beta = 1$, $\omega_0 = 1$, and $\Delta\omega = 0.2$.

TSS without fluctuations of the natural frequencies

Here we show that the fluctuations of the natural frequencies are unnecessary to realize the TSS as in conventional chimera states [26, 27]. We calculate the dynamics of the first model of the TSS (Eq. (1) in the main text and Supplementary Eq. (S1)) without fluctuations of natural frequencies, i.e., $\Delta\omega = 0$. Supplementary Figure S3 presents the frequency distribution obtained under the homogeneous natural frequency. We can confirm that the edge oscillators vibrate at a homogeneous and constant frequency, while the bulk oscillators exhibit inhomogeneous and unstable frequencies. Therefore, the TSS appears even under

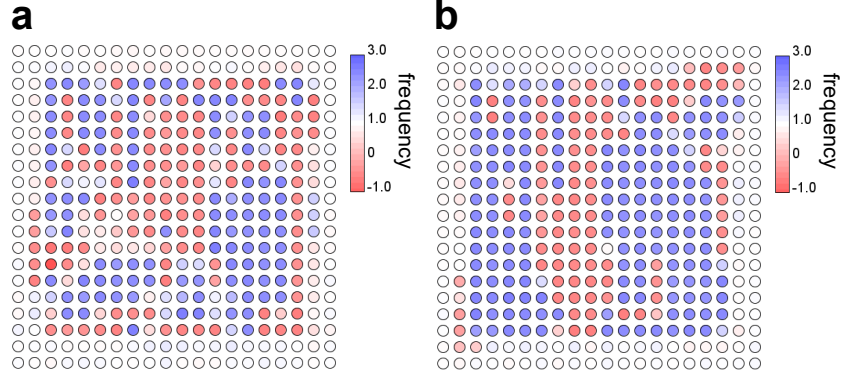


FIG. S3. TSS without fluctuations of the natural frequencies. **a,b** We simulate the first model of the TSS (Eq. (1) in the main text and Supplementary Eq. (S1)) under the condition of the homogeneous natural frequencies. Panel **a** (**b**) shows the snapshot of the frequency distribution of the first component of oscillators at the time $t = 100$ ($t = 200$). As in the case of the fluctuating natural frequencies (Fig. 1c,d in the main text), the edge oscillators exhibit homogeneous and constant frequencies, while the bulk ones vibrate at space- and time-varying frequencies. Therefore, the edge oscillators synchronize, while the bulk ones desynchronize, which indicates the emergence of the TSS. The parameters used are $u = -1$, $b = 0.5$, $\alpha = 0.5$, $\beta = 1$, $\omega_0 = 1$, and $\Delta\omega = 0$.

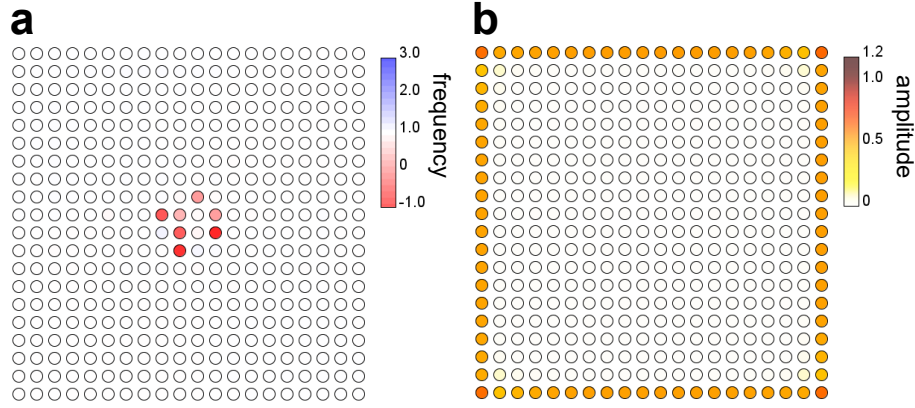


FIG. S4. Coexistence of synchronized edge oscillators and damped bulk oscillators. **a** The frequency of the first component of oscillators at each site is presented in a damping parameter region. We numerically simulate the first model of the TSS (Eq. (1) in the main text and Supplementary Eq. (S1)) at the parameters $u = -1$, $b = 0.5$, $\alpha = -0.2$, $\beta = 1$, $\omega_0 = 1$, and $\Delta\omega = 0$. The figure shows the snapshot at time $t = 100$. The edge oscillators exhibit homogeneous frequencies and thus synchronize. **b** The amplitudes of the first components of oscillators at each site at time $t = 100$ are shown. We can confirm that the bulk oscillators exhibit almost zero amplitudes. The parameters used are the same as in panel **a**.

the homogeneous natural frequency. We set the parameters as $u = -1$, $b = 0.5$, $\alpha = 0.5$, $\beta = 1$, and $\omega_0 = 1$ and consider the random initial condition as in Fig. 1 in the main text.

Coexistence of synchronized edge oscillators and damped bulk ones

By tuning the parameters, we show that our model (Eq. (1) in the main text and Supplementary Eq. (S1)) can exhibit a different coexistence state of synchronization where the bulk oscillators are damped while the edge ones are synchronized. Here, we set the parameter α in the Stuart-Landau equation (cf. Eq. (1) in the main text) to be negative and larger than $-|b|$. The negativity of α implies the damping of self-oscillations of the bulk oscillators, while the lasing edge modes of linear couplings still lead to synchronized oscillations at the edge of the sample in this parameter region. Supplementary Figure S4 shows the frequency and amplitude distributions obtained from the numerical calculations of our model at $\alpha = -0.2$. We can confirm that the bulk oscillators exhibit almost zero amplitudes, while the edge ones synchronize. It is noteworthy that the bulk oscillators slightly oscillate at frequencies close to that of the edge ones due to their interaction. We define the TSS as the coexistence of the synchronized edge oscillators and the desynchronized bulk oscillators, while the synchronized state observed in this calculation

exhibits bulk oscillators without self-oscillations and thus is not categorized in the TSS.

Stability of the TSS via a one-dimensional model

Here we discuss the stability of the TSS via the one-dimensional chain of Stuart-Landau oscillators which effectively describes the edge oscillators in our first model (Eq. (1) in the main text and Supplementary Eq. (S1)). Since the edge oscillators in our model exhibit larger amplitudes than those of the bulk ones (cf. Fig. 1e in the main text), the interaction between the edge and bulk oscillators is smaller than that between the edge ones. Therefore, we can assume that the linear couplings between the edge and bulk oscillators only have a perturbative effect on the dynamics of the synchronized edge oscillators, and thus the model without the hopping terms in the x direction,

$$\frac{d}{dt}Z_j(y) = (i\omega_j(y) + \alpha - \beta|Z_j(y)|^2)Z_j(y) - i \sum_{k,y'} H_{jk}^{1d}(y, y')Z_k(y') + \xi_j(y), \quad (\text{S7})$$

$$H_{jk}^{1d}(y, y') = \left(u\delta_{y,y'} + \frac{\delta_{y+1,y'} + \delta_{y-1,y'}}{2} \right) (I_2 \otimes \sigma_z)_{jk} + i \frac{\delta_{y+1,y'} - \delta_{y-1,y'}}{2} (I_2 \otimes \sigma_y)_{jk} + ib\delta_{y,y'}(\sigma_x \otimes \sigma_x)_{jk} \quad (\text{S8})$$

can describe the edge oscillators in our first model, where $\delta_{y,y'}$ is the Kronecker delta and σ_i and I_2 are the i th component of the Pauli matrices and the 2×2 identity matrix respectively. We introduce $\xi_j(y)$ to describe the perturbative effect from the bulk

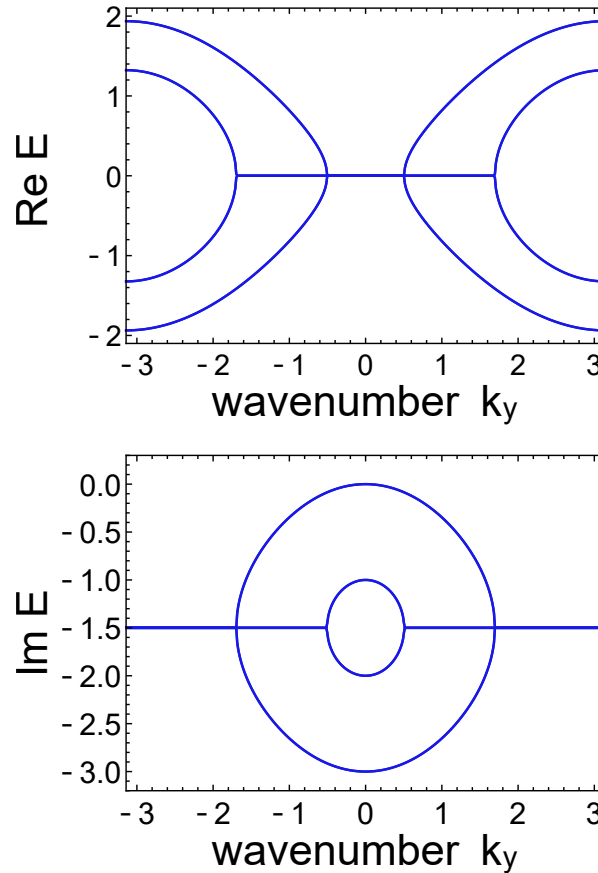


FIG. S5. Dispersion relation of the linearized equation of one-dimensional chain model. We numerically calculate the dispersion relation of the coefficient matrix obtained from the linearization of the one-dimensional chain model around the stationary solution (Supplementary Eqs. (S9), (S10)). The upper (lower) panel shows the real (imaginary) part of the eigenvalues. All the eigenvalues have nonpositive imaginary parts, which implies the linear stability of the stationary solution. The parameters used are $u = -1$, $b = 0.5$, $\alpha = 0.5$, $\beta = 1$, $\omega_0 = 0$, and $\Delta\omega = 0$.

oscillators, while we show that the TSS is robust against such perturbation and inhomogeneity of parameters. We note that the chaotic dynamics in the bulk vanishes the long-term correlation of interaction between the edge and bulk oscillators, and thus $\xi_j(y)$ can be considered as noise.

First, we obtain the stationary synchronized solution of Supplementary Eq. (S7) under the absence of the interaction from bulk oscillators and the homogeneous natural frequencies. We conduct the Fourier transformation of the Hamiltonian used in the one-dimensional model (Supplementary Eq. (S8)) and obtain

$$H^{1d}(k) = (u + \cos k_y) I_2 \otimes \sigma_z + \sin k_y I_2 \otimes \sigma_y + ib \sigma_x \otimes \sigma_x. \quad (S9)$$

This Hamiltonian exhibits the maximum imaginary part of the eigenenergies $\text{Im } E = \sqrt{b^2 - u'^2}$ at $k_y = 0$ and the corresponding eigenvector $(ib, \mp u' \pm i\sqrt{b^2 - u'^2}, \pm ib, -u' + i\sqrt{b^2 - u'^2})^T$, where $u' = u + 1$. By utilizing this eigenvector, we construct the following homogeneous stationary (periodic) solution:

$$\begin{pmatrix} Z_1(y) \\ Z_2(y) \\ Z_3(y) \\ Z_4(y) \end{pmatrix} = e^{i\omega_0 t + i\theta} \sqrt{\frac{\alpha + \sqrt{b^2 - u'^2}}{b^2 \beta}} \begin{pmatrix} ib \\ \mp u' \pm i\sqrt{b^2 - u'^2} \\ \pm ib \\ -u' + i\sqrt{b^2 - u'^2} \end{pmatrix}, \quad (S10)$$

where ω_0 is the homogeneous natural frequency. Since the gapped bulk bands require $|u'| < |b|$, the absolute values of the components of this stationary solution are the same, which leads to the same intensity of the nonlinear terms. The stationary solution (Supplementary Eq. (S10)) represents the synchronization of the edge oscillators, where they oscillate at the same frequency ω_0 .

To confirm the stability of the synchronization of the edge oscillators, we conduct linear stability analysis around the stationary solution (Supplementary Eq. (S10)). We linearize the Stuart-Landau equation $\dot{Z} = (i\omega + \alpha - \beta Z^2)Z$ and obtain

$$\frac{d}{dt} \begin{pmatrix} \delta X \\ \delta Y \end{pmatrix} = \begin{pmatrix} i\omega + \alpha - 3\beta X_0^2 - \beta Y_0^2 & -2\beta X_0 Y_0 \\ -2\beta X_0 Y_0 & i\omega + \alpha - \beta X_0^2 - 3\beta Y_0^2 \end{pmatrix} \begin{pmatrix} \delta X \\ \delta Y \end{pmatrix}, \quad (S11)$$

where $Z = X + iY$ (X, Y are real) and $Z_0 = X_0 + iY_0$ is the state around which the equation is linearized. The eigenvalues of the coefficient matrix in this equation are $i\omega + \alpha - X_0^2 - Y_0^2$, $i\omega + \alpha - 3X_0^2 - 3Y_0^2$ and have negative real parts when we linearize the equation around the stationary solution (Supplementary Eq. (S10)). Therefore, these terms attenuate the fluctuations from the stationary solution, which leads to the linear stability of the one-dimensional chain of nonlinear oscillators. We numerically diagonalize the linearized equation of Supplementary Eq. (S7) and obtain the dispersion relation in Supplementary Fig. S5. We confirm that all the eigenvalues have nonpositive imaginary parts, which indicates the linear stability of the stationary solution. Therefore, the synchronized state in the one-dimensional model (Supplementary Eq. (S7)) is robust against the perturbations, such as the inhomogeneity of the natural frequencies and the perturbative interactions from bulk ones. Since the one-dimensional chain of oscillators and its stationary solution describes the synchronized edge oscillators in our first model (Eq. (1) in the main text and Supplementary Eq. (S1)), the TSS is also stable against the existence of disorders.

Lyapunov analysis on the model of TSS utilizing conventional topological edge modes

Here, we analyze the chaotic behavior of the model utilizing edge modes protected by conventional bulk topology (cf. Supplementary Eq. (S4)). The Hamiltonian used to describe the linear couplings is

$$\begin{aligned} H(\mathbf{k}) &= \begin{pmatrix} aH_{\text{QWZ}} & ibI_2 \\ ibI_2 & H_{\text{QWZ}} \end{pmatrix} \\ &= (u + \cos k_x + \cos k_y) \left[\frac{a+1}{2} (I_2 \otimes \sigma_z) + \frac{a-1}{2} (\sigma_z \otimes \sigma_z) \right] \\ &\quad + \sin k_y \left[\frac{a+1}{2} (I_2 \otimes \sigma_y) + \frac{a-1}{2} (\sigma_z \otimes \sigma_y) \right] \\ &\quad + \sin k_x \left[\frac{a+1}{2} (I_2 \otimes \sigma_x) + \frac{a-1}{2} (\sigma_z \otimes \sigma_x) \right] + ib(\sigma_x \otimes I_2) + iu'(\sigma_z \otimes I_2) \end{aligned} \quad (S12) \quad (S13)$$

in the wavenumber space, where H_{QWZ} is the Hamiltonian of the Qi-Wu-Zhang model [53] and $I_2, \sigma_{x,y,z}$ are the 2×2 identity matrix and the Pauli matrices respectively. This Hamiltonian exhibits nonzero Chern numbers and lasing edge modes, i.e.,

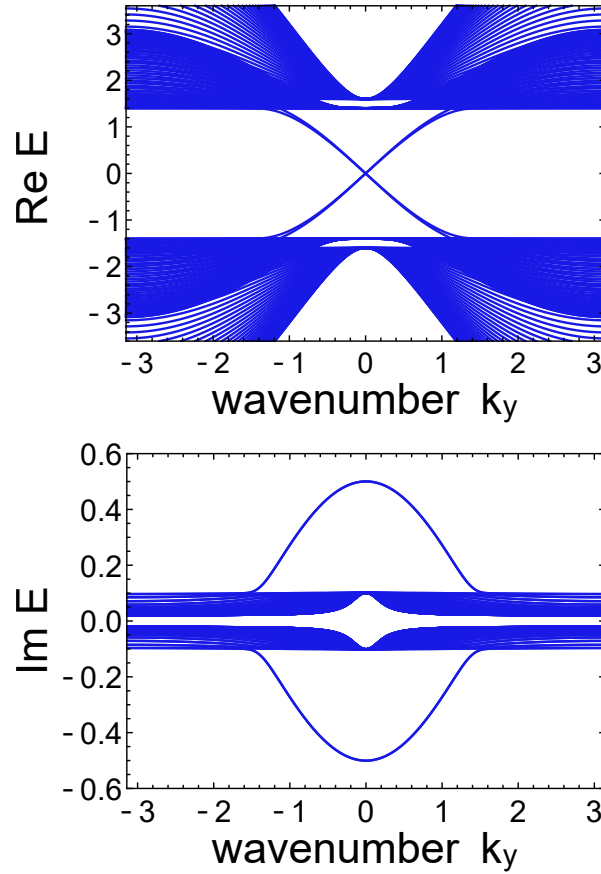


FIG. S6. Band structure of lasing edge modes protected by conventional bulk topology. The band structure of the Hamiltonian of lasing edge modes (Supplementary Eqs. (S4), (S13)) is shown. There exist gapless edge modes with larger imaginary parts of eigenvalues than those of the bulk modes. The parameters used are $u = -1$, $u' = 0.02$, $a = 2$, and $b = 0.5$.

gapless localized modes with the positive imaginary parts of the eigenvalues. We confirm the existence of such edge modes by calculating the dispersion relation under the open (periodic) boundary condition in the x (y) direction. Supplementary Figure S6 shows the dispersion relation of the lasing edge modes. One can find the gapless modes with positive imaginary parts of eigenvalues larger than those of the bulk modes. As discussed in the main text, these edge modes lead to the TSS in the linearly coupled Stuart-Landau oscillators (cf. Fig. 3 in the main text).

We also calculate the Lyapunov exponents and vectors to confirm the chaos of the bulk oscillators and the existence of the edge-localized Lyapunov vectors. We use the Shimada-Nashima algorithm [54] and Ginelli's algorithm [55] as in Fig. 4 in the main text. We set the time step and the initialization period as $\Delta t = 0.1$ and $T_{\text{ini}} = 1000$ for each, and obtain the trajectory from $t = T_{\text{ini}}$ to $t = T_{\text{ini}} + 20000$ in a 10×10 square lattice. To omit the effect of the initial condition, we use the R matrices obtained from the time $t = T_{\text{ini}} + 10000$ to $t = T_{\text{ini}} + 20000$ to calculate the Lyapunov exponents and vectors. Supplementary Figure S7a shows the Lyapunov exponents of the model considered here. There are positive Lyapunov exponents which indicate the chaos of the bulk oscillators.

Supplementary Figure S7b shows the proportions of the edge amplitudes (Eq. (2) in the main text) of the Lyapunov exponents. We can confirm the existence of the edge-localized Lyapunov vectors as in the model using exceptional edge modes [41] (cf. Supplementary Eq. (S1) and Fig. 4b in the main text). However, the behavior of the inverse participation ratios (IPRs) (Eq. (3) in the main text) shown in Supplementary Fig. S7c is different from that in Fig. 4c in the main text, because there are no steep increases in the IPRs. Thus, the strongly localized Lyapunov vectors disappear from the model considered here. This is because the nonlinear effects are not large enough to generate such strongly localized modes. We also note that nonlinearity-induced boundary modes are absent in this model as can be seen in Fig. 5 in the main text. This may also be due to the smallness of nonlinearity.

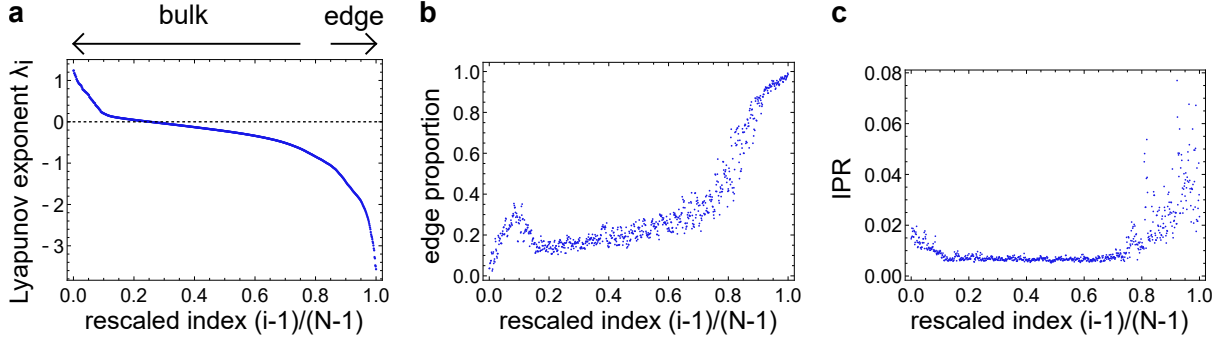


FIG. S7. Lyapunov analysis of the model of TSS utilizing lasing edge modes protected by conventional bulk topology. **a** We calculate the Lyapunov exponents of the model with the linear couplings exhibiting edge modes protected by conventional bulk topology (Supplementary Eq. (S4), (S13)). The index of each Lyapunov exponent is rescaled for the maximum to be unity. We obtain positive Lyapunov exponents (above the dashed line) as in Fig. 4 in the main text, which indicates the chaos of the bulk oscillators. The parameters used are $u = -1$, $u' = 0.02$, $a = 2$, $b = 0.5$, $\alpha = 0.5$, $\beta = 1$, $\omega_0 = 0.2$, and $\Delta\omega = 0.2$. **b** The proportions of the edge amplitudes P_{edge} (Eq. (2) in the main text) of the Lyapunov vectors are shown. We set the relative index of the Lyapunov vector to be the same as panel **a**. The edge proportions rise steeply around the relative index 0.8, which indicates that the Lyapunov vectors of the small indices spread in the bulk, while those of the large indices are localized at the edge of the system. **c** Inverse participation ratios (IPRs) of the Lyapunov vectors are presented. We set the relative index of the Lyapunov vector to be the same as in panel **a**. The IPRs increase around the relative index 0.8, corresponding to the edge localization of the Lyapunov vectors. Since all the IPRs are less than 0.08, the strongly localized modes are absent unlike Fig. 4 in the main text.

TSS in nonidentical oscillators with Hermitian linear couplings

Here we show that the TSS can emerge in nonidentical nonlinear oscillators with linear couplings described by a Hermitian Hamiltonian. We consider the unitary transformation of the Hamiltonian considered in the main text (cf. Supplementary Eq. (S1)) and obtain

$$H(\mathbf{k}) = (u + \cos k_x + \cos k_y)\sigma_x \otimes \sigma_z + \sin k_y I_2 \otimes \sigma_y + \sin k_x I_2 \otimes \sigma_x + ib\sigma_z \otimes \sigma_z, \quad (\text{S14})$$

where I_2 is the 2×2 identity matrix and $\sigma_{x,y,z}$ are the Pauli matrices. This Hamiltonian is described in the real space as

$$H_{jk}(\mathbf{x}, \mathbf{x}') = \left(u\delta_{\mathbf{x}, \mathbf{x}'} + \frac{\delta_{\mathbf{x}+\mathbf{e}_x, \mathbf{x}'} + \delta_{\mathbf{x}-\mathbf{e}_x, \mathbf{x}'} + \delta_{\mathbf{x}+\mathbf{e}_y, \mathbf{x}'} + \delta_{\mathbf{x}-\mathbf{e}_y, \mathbf{x}'}}{2} \right) (\sigma_x \otimes \sigma_z)_{jk} \\ + i \frac{\delta_{\mathbf{x}+\mathbf{e}_y, \mathbf{x}'} - \delta_{\mathbf{x}-\mathbf{e}_y, \mathbf{x}'}}{2} (I_2 \otimes \sigma_y)_{jk} + i \frac{\delta_{\mathbf{x}+\mathbf{e}_x, \mathbf{x}'} - \delta_{\mathbf{x}-\mathbf{e}_x, \mathbf{x}'}}{2} (I_2 \otimes \sigma_x)_{jk} + ib\delta_{\mathbf{x}, \mathbf{x}'} (\sigma_z \otimes \sigma_z)_{jk}, \quad (\text{S15})$$

where $\delta_{\mathbf{x}, \mathbf{x}'}$ is the Kronecker delta and $\mathbf{e}_{x,y}$ are the lattice vectors in the x or y direction. We note that the non-Hermitian term in this Hamiltonian is $ib\delta_{\mathbf{x}, \mathbf{x}'} (\sigma_z \otimes \sigma_z)_{jk}$, which is introduced as the modulation of the parameter α in the Stuart-Landau equation (cf. Eq. (1) in the main text). Thus, we can consider Stuart-Landau oscillators with this linear coupling as nonidentical oscillators whose linear coupling is Hermitian. We numerically calculate the dynamics of such coupled nonidentical oscillators. Supplementary Figure S8a shows the frequency distribution of oscillators at the first components of lattice points. We confirm the TSS, i.e., the edge oscillators synchronize while the bulk ones exhibit chaos. Unlike the other models of TSS, however, the second components of the oscillators exhibit chaotic motion even at the edge of the system (Supplementary Fig. S8c). Such synchronization and desynchronization of the edge oscillators can be confirmed from the indicator of the local order parameter restricted to the first and fourth (second and third) components

$$M(x, y; t) = \frac{1}{2T} \int_{t-T}^t dt' \sum_{k=1,4 \text{ (or } k=2,3)} |Z_k(x, y) + Z_k(x+1, y) + Z_k(x-1, y) + Z_k(x, y+1) + Z_k(x, y-1)|, \quad (\text{S16})$$

as shown in Supplementary Fig. S8b,d. The first components of edge oscillators exhibit large indicators of the local order parameter indicating their synchronization, while those of the second components have small values.

We also calculate the Lyapunov exponents and vectors to confirm the chaos of the bulk oscillators as in Fig. 4 in the main text and Supplementary Fig. S9. Unlike Fig. 4 and Supplementary Fig. S9, we set the initialization period as $T_{\text{ini}} = 100000$. Supplementary Figure S9a shows the existence of positive Lyapunov exponents, which implies the chaos in this system. We compare the proportion of amplitude of the edge oscillators of the Lyapunov vectors (cf. Eq. (2) in the main text) between the first and fourth components and the second and third ones, as shown in Supplementary Fig. S9b,c. The Lyapunov vectors

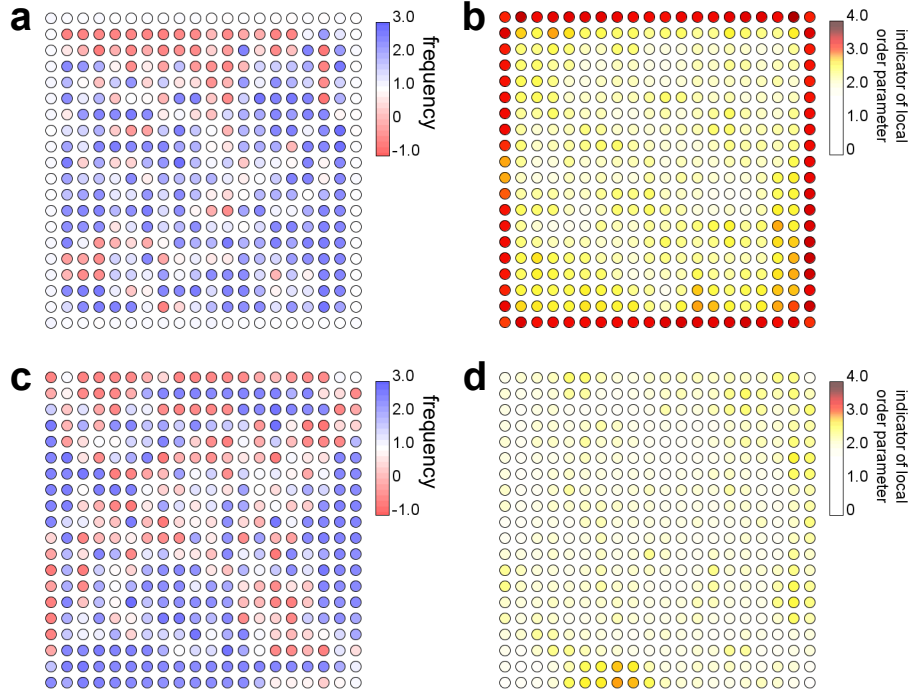


FIG. S8. Frequency and amplitude distributions of the model utilizing Hermitian linear couplings. **a-d** We numerically simulate the model utilizing Hermitian linear couplings (Supplementary Eq. (S14)). The frequency (**a,c**) and the indicator of the local order parameter $M(x, y)$ (Eq. (4) in the main text, **b,d**) at each site are shown. Panel **a,b** (**c,d**) presents the frequencies and the indicators of the local order parameters of the first (second) component of oscillators at time $t = 100$. The edge oscillators at the first components of the lattice points exhibit the homogeneous and constant frequency and the large indicators of the local order parameters, which implies their synchronization. In contrast, the second components of oscillators are desynchronized. The parameters used are $u = -1$, $b = 0.5$, $\alpha = 1$, $\beta = 1$, $\omega_0 = 1$, and $\Delta\omega = 0.2$.

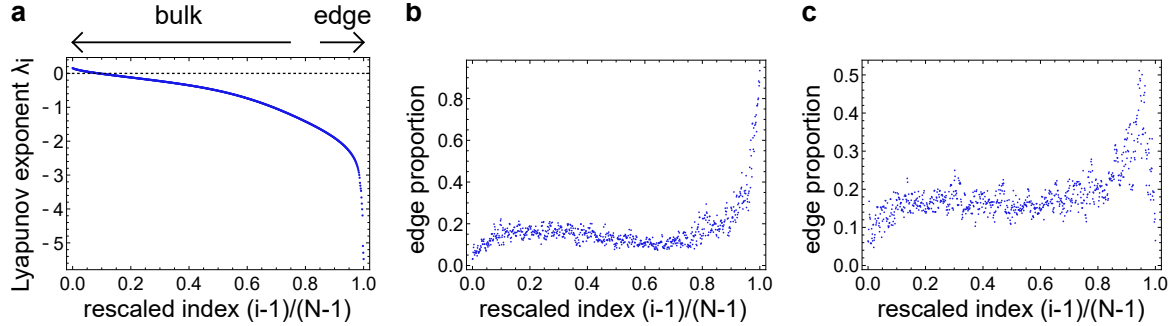


FIG. S9. Lyapunov analysis of the model utilizing Hermitian linear couplings. **a** The Lyapunov exponents of the model with the Hermitian linear couplings (Supplementary Eq. (S14)) are plotted in descending order. The index of each Lyapunov exponent is rescaled for the maximum to be unity. Positive Lyapunov exponents (above the dashed line) exist as in Fig. 4 in the main text, indicating the chaos of the bulk oscillators. The parameters used are $u = -1$, $b = 0.5$, $\alpha = 1$, $\beta = 1$, $\omega_0 = 0.2$, and $\Delta\omega = 0.2$. **b,c** The proportions of the edge amplitudes P_{edge} (Eq. (2) in the main text) of the first and fourth (second and third) components of the Lyapunov vectors are shown in panel **b** (**c**). We set the relative index of the Lyapunov vector to be the same as panel **a**. The edge proportions of the first and fourth components rise steeply around the relative index 0.95, which indicates that the Lyapunov vectors of the large indices are localized at the first and fourth components of the edge sites. On the other hand, the edge proportion of the second and third components decrease in that region around the relative index 0.95. Therefore, the second and third components of the edge oscillators exhibit chaotic behavior.

corresponding to small Lyapunov exponents are localized at the first and fourth components of the edge sites. On the other hand, the amplitudes of Lyapunov exponents at the second and third components are small at the large indices. Thus, the first and fourth components of edge oscillators are synchronized, while the other oscillators exhibit chaos.

Desynchronization of the second and third components of the edge oscillators is explained from the amplitude distribution of the lasing edge modes shown in Supplementary Fig. S10. The lasing edge modes with the maximum imaginary part of the eigenvalue exhibit zero amplitude at the second and third components of the lattices and edge-localized amplitudes at the first

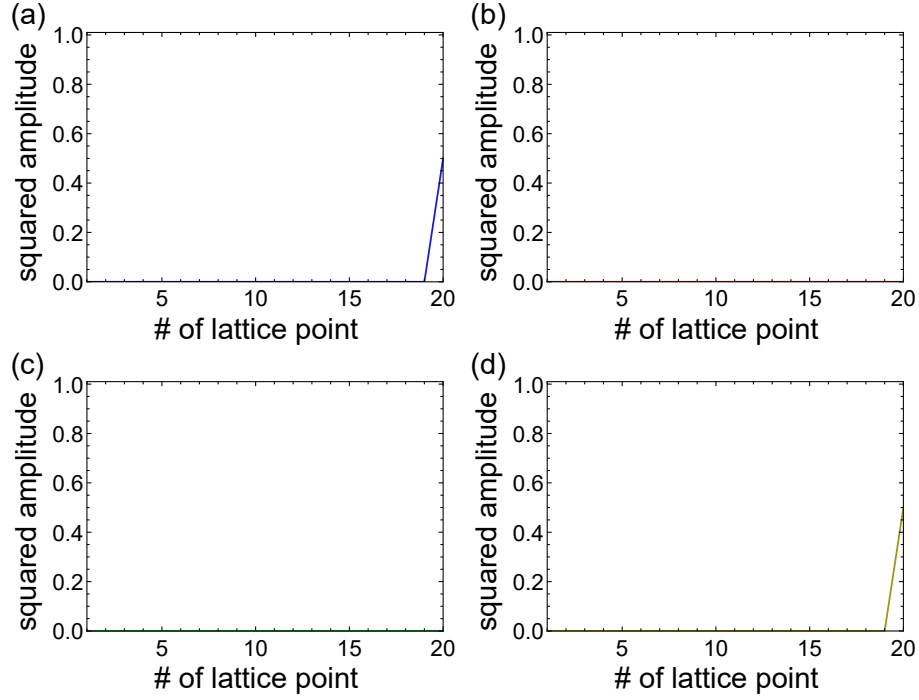


FIG. S10. Amplitude distribution of the lasing edge modes. **a-d** The squared amplitude of the lasing edge mode of the linear couplings (Supplementary Eq. (S14)) is shown. The wavenumber is $k = 0$ and the eigenvalue is $E = ib$. Panels **a**, **b**, **c**, and **d** show the amplitude distributions of the first, second, third, and fourth components for each. The amplitudes of lasing edge modes are localized at the first and fourth components. The parameters used are $u = -1$ and $b = 0.5$.

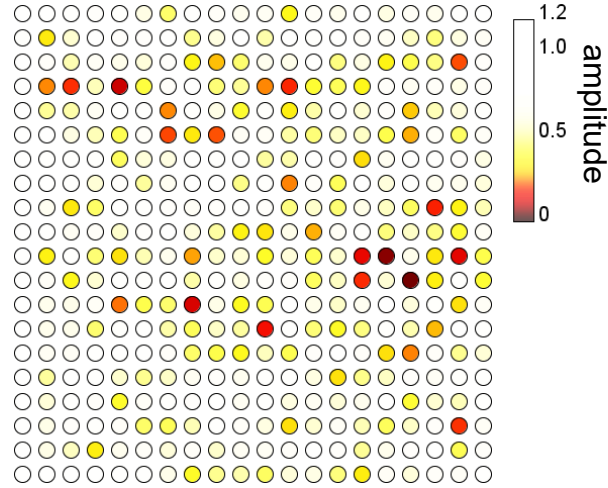


FIG. S11. **Amplitude distribution indicating amplitude chaos.** The amplitudes of oscillators at the first components of lattice points are shown. To obtain the amplitude distribution, we numerically calculate the dynamics of the first model of TSS (cf. Eq. (1) in the main text and Supplementary Eq. (S1)). The red-filled circles represent the site with small amplitudes. The existence of such small-amplitude oscillators indicates amplitude chaos. The parameters used are $u = -1$, $b = 0.5$, $\alpha = 0.5$, $\beta = 1$, $\omega_0 = 1$, and $\Delta\omega = 0.2$.

and fourth components. Therefore, the lasing edge modes obtained from the linear coupling (Supplementary Eq. (S14)) only amplifies the first and fourth components of the edge oscillators. Since such amplification leads to the different behavior between the edge and bulk oscillators (see also the previous section), only the first and fourth components of the edge oscillators can synchronize, while the second and third components exhibit chaotic oscillations.

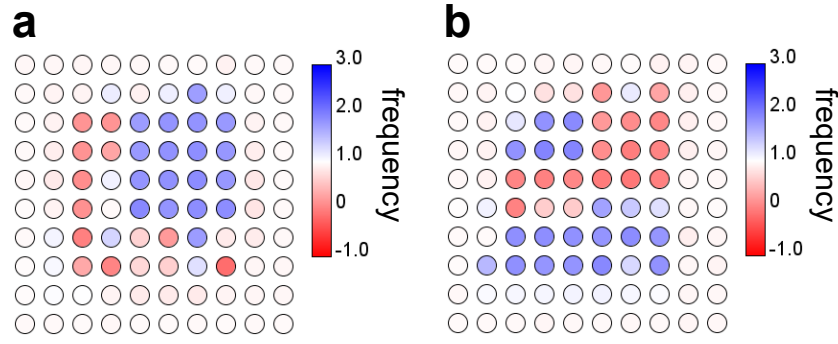


FIG. S12. Frequency distribution of the model of the TSS in a 10×10 lattice. **a,b** We numerically simulate the first model of the TSS (Eq. (1) in the main text and Supplementary Eq. (S1)) in a smaller lattice than that considered in Fig. 1 in the main text. Here, we arrange 10×10 sites and consider the open boundary condition. Panel **a** (**b**) shows the snapshot of the frequency distribution of the first component of oscillators at the time $t = 100$ ($t = 200$). As in the 20×20 lattices (Fig. 1 in the main text), the edge oscillators exhibit homogeneous and constant frequencies, while the bulk ones vibrate at space- and time-varying frequencies. Therefore, the edge oscillators synchronize, while the bulk ones desynchronize, which indicates the emergence of the TSS. The parameters used are $u = -1$, $b = 0.5$, $\alpha = 0.5$, $\beta = 1$, $\omega_0 = 1$, and $\Delta\omega = 0.2$.

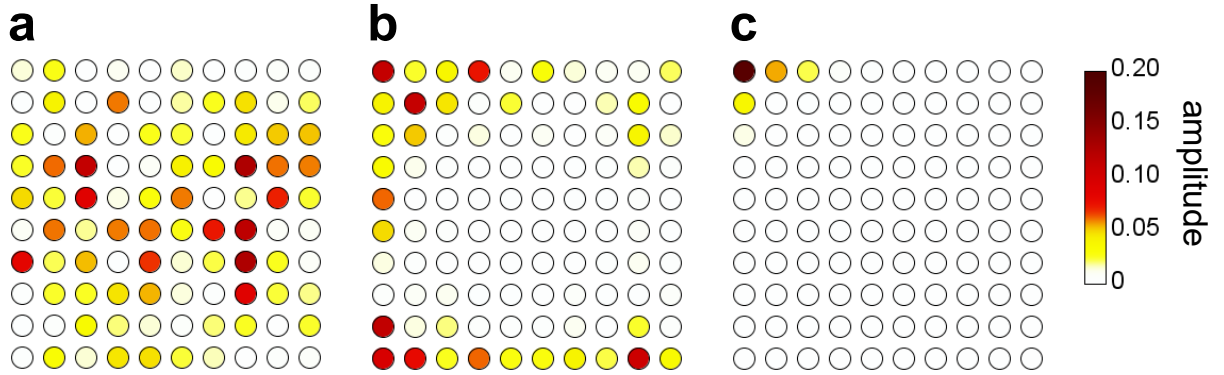


FIG. S13. Amplitude distributions of the Lyapunov vectors. **a-c** The absolute values of the first components of the Lyapunov vectors at each site are plotted in 10×10 square lattices. **a** The Lyapunov vector associated with a positive Lyapunov exponent (the index $n = 50$) is shown. One can confirm that the bulk sites exhibit large amplitudes. **b** The Lyapunov vector of the index $n = 700$ is shown. We can see its localization to the edge of the system. **c** The Lyapunov vectors associated with the smallest Lyapunov vectors (the index $n = 800$) is shown. It is strongly localized to the upper-left corner. Thus, most of the sites have small amplitudes.

Amplitude chaos in the TSS

Amplitude oscillators such as Stuart-Landau oscillators can exhibit two types of chaos, amplitude chaos and phase chaos. Amplitude chaos [44] accompanies phase slips where the amplitudes of oscillators go to zero, and thus the phases jump. Such amplitude-dependent behavior is unique to amplitude oscillators and thus cannot be described by their phase equations.

We confirm the amplitude chaos in our first model (cf. Eq. (1) in the main text and Supplementary Eq. (S1)). We numerically calculate the dynamics of our model as in Fig. 1 in the main text. Supplementary Figure S11 plots the amplitudes of the first component at each site and emphasizes the sites with small amplitudes. A part of bulk oscillators exhibit almost zero amplitudes, and thus phase slips can occur. Therefore, amplitude chaos appears in the bulk of our model. We note that our model can also exhibit the phase chaotic behavior (i.e. chaos irrelevant to the phase slips observed in the numerical calculation).

Real-space distribution of frequencies and Lyapunov vectors in a 10×10 square lattice

Related to the calculation in Fig. 4 in the main text, we calculate the dynamics of the first model (cf. Eq. (1) in the main text and Supplementary Eq. (S1)) of the TSS in a 10×10 square lattice. Supplementary Figure S12 shows snapshots of the frequencies of oscillators. We can confirm the synchronization of the edge oscillators and the desynchronization of the bulk oscillators. We

thus expect that the TSS can appear independently of the system size.

We also calculate the Lyapunov vectors [24, 55] in the 10×10 lattice model and find that some of them are localized to the edge of the system (cf. Fig. 4b,c in the main text). Here we plot the Lyapunov vectors in the real space and directly demonstrate such localization of the Lyapunov vectors. Supplementary Figure S13 shows some examples of Lyapunov vectors. One can see that the Lyapunov vector associated with a positive Lyapunov exponent (corresponding to Supplementary Fig. S13a) has large amplitudes at a large number of bulk sites. Meanwhile, most of the bulk sites have small amplitudes in the Lyapunov vector of the relative index around 0.875 (corresponding to Supplementary Fig. S13b), which indicates its localization to the edge. Furthermore, the Lyapunov vector of the largest index is strongly localized to corner sites as shown in Supplementary Fig. S13c, which leads to the large value of its inverse participation ratio (see Eq. (3) and Fig. 4c in the main text). Thus, these observations of the Lyapunov vectors in the real space are consistent with the results in Fig. 4 in the main text.

Dispersion relation of the effective Hamiltonian

Here we calculate the dispersion relation of the effective Hamiltonian derived from the linearization of the equation of our first model (Eq. (1) in the main text and Supplementary Eq. (S1)). Such effective Hamiltonian includes the on-site loss induced by the nonlinear terms, which depends on the state around which the linearization is performed. Specifically, such on-site loss terms are obtained from the linearization of the Stuart-Landau oscillators $\dot{Z} = (i\omega + \alpha - \beta Z^2)Z$ as

$$\frac{d}{dt} \begin{pmatrix} \delta X \\ \delta Y \end{pmatrix} = \begin{pmatrix} i\omega + \alpha - 3\beta X_0^2 - \beta Y_0^2 & -2\beta X_0 Y_0 \\ -2\beta X_0 Y_0 & i\omega + \alpha - \beta X_0^2 - 3\beta Y_0^2 \end{pmatrix} \begin{pmatrix} \delta X \\ \delta Y \end{pmatrix}, \quad (\text{S17})$$

where $Z = X + iY$ (X, Y are real) and $Z_0 = X_0 + iY_0$ is the state around which the equation is linearized. We note that the coefficient matrix in this equation has eigenvalues $i\omega + \alpha - X_0^2 - Y_0^2$, $i\omega + \alpha - 3X_0^2 - 3Y_0^2$. Thus, if the square of the

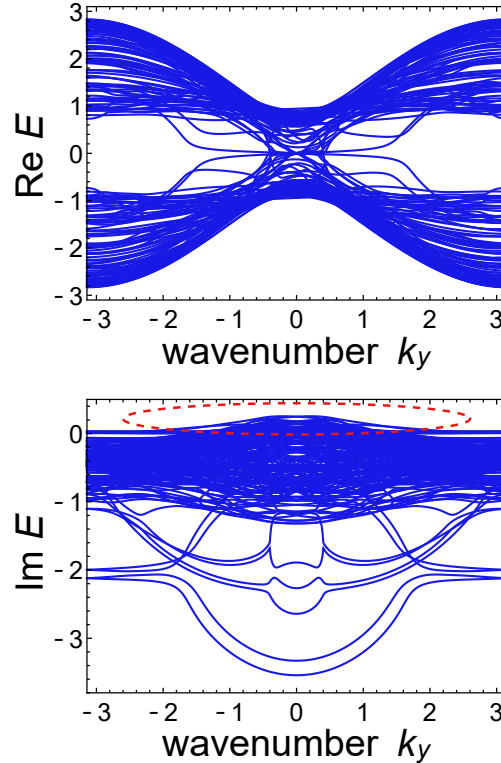


FIG. S14. Dispersion relation of the effective Hamiltonian. We calculate the dispersion relation of the effective Hamiltonian obtained from the linearization of the first model (cf. Eq. (1) in the main text and Supplementary Eq. (S1)). We consider the open (periodic) boundary condition in the x (y) direction and arrange 20 sites in the x direction. While the bulk bands are gapless as opposed to conventional topological systems, the edge localized modes still exist in this dispersion relation. The edge modes exhibit negative imaginary parts of the eigenvalues. In contrast, some bulk modes possess positive imaginary parts of the eigenvalues depicted by the red dashed circle, which indicates instability of the bulk oscillators. The parameters used are $u = -1$, $b = 0.5$, $\alpha = 0.5$, $\beta = 1$, $\omega_0 = 1$, and $\Delta\omega = 0$.

amplitude is $X_0^2 + Y_0^2 = \alpha/\beta$ (equal to the amplitude of the isolated Stuart-Landau oscillator), the obtained on-site term leads to attenuation of the fluctuation.

To determine the intensities of those on-site loss terms, we first simulate the dynamics of our first model (Eq. (1) in the main text and Supplementary Eq. (S1)) in a 20×20 square lattice under the periodic (open) boundary condition in the x (y) direction. Here we consider the random initial condition as in Fig. 1 in the main text. We obtain the state variables of the oscillators in the 10th row at $t = 200$ and linearize the equation around them. In the calculation of the dispersion relation, we consider a 1×20 supercell structure. Finally, we numerically diagonalize the obtained effective Hamiltonian and plot the dispersion relation as shown in Supplementary Fig. S14. We find bulk modes exhibiting positive imaginary parts of eigenvalues, which lead to the chaotic dynamics of the bulk oscillators. There are also gapless modes with negative imaginary parts of eigenvalues that are localized at the edge of the sample. These edge modes should correspond to the edge-localized Lyapunov vectors in our first model (cf. Fig. 4 in the main text and Supplementary Fig. S13). We note that the non-Hermiticity of the effective Hamiltonian plays an important role, because nonzero imaginary parts of eigenvalues correspond to nonzero Lyapunov exponents and are unique to non-Hermitian Hamiltonians. It is also noteworthy that the bulk bands with the positive imaginary parts of the eigenvalues are derived from the repulsion of the bulk bands of the original linear couplings with zero imaginary parts (cf. Supplementary Figs. S6, S16). To realize such degenerated imaginary bulk bands and lasing edge modes, (at least) four oscillators seem to be necessary at each site.

While nonlinearity generates random on-site loss terms in the effective Hamiltonian, topological modes are robust against such disorder. Especially, previous research [41] shows that the edge modes of the Hamiltonian describing the linear coupling of our first model (cf. Supplementary Eq. (S1)) are robust against perturbative on-site gain and loss. In contrast to conventional topological insulators, the bulk bands are also gapless in Supplementary Fig. S14. However, the edge and bulk modes are not degenerate, and thus edge modes remain in the effective Hamiltonian. We note that the state-dependent Hamiltonian analyzed in Fig. 5a,b in the main text also includes random on-site loss terms, while they have no effects on the robust existence of the topological modes in the state-dependent Hamiltonian.

We note that the imaginary parts of the eigenvalues of the effective Hamiltonian represent the short-term stability or instability of the system, while the Lyapunov exponents represent the long-term stability or instability. The Lyapunov exponents and vectors correspond to the time-averaged behavior of the effective Hamiltonian and thus are different from the eigenvalues and eigenvectors of the effective Hamiltonian obtained at each period. However, since the edge modes are robust against the unsteady disordered effect of nonlinear terms, the edge-localized modes and their dissipative behaviors remain even after the time averaging.

Inverse participation ratios of the Lyapunov vectors in the wavenumber space

While in the main text we analyze the inverse participation ratios (IPRs) of the Lyapunov vectors in the real space, here we calculate and discuss the IPRs of our first model (cf. Eq. (1) in the main text and Supplementary Eq. (S1)) in the wavenumber space. Especially, we find that the IPRs in the wavenumber space classify the bulk-extended Lyapunov vectors into two groups. To obtain the IPRs in the wavenumber space, we conduct the Fourier transformation of the Lyapunov vectors of our model, and

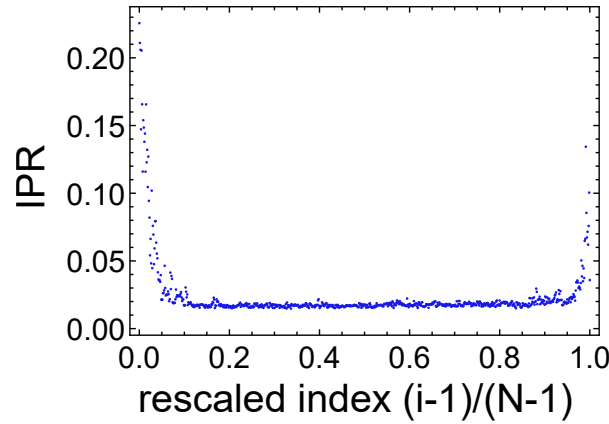


FIG. S15. Inverse participation ratios of the Lyapunov vectors in the wavenumber space. We numerically calculate and plot the inverse participation ratios of the Fourier components of the Lyapunov vectors obtained from the model of the TSS (Eq. (1) in the main text). The relative indices correspond to those in Fig. 4 in the main text. We confirm the large IPRs at small relative indices (smaller than about 0.05) and large relative indices (larger than about 0.95). The parameters used are $u = -1$, $b = 0.5$, $\alpha = 0.5$, $\beta = 1$, $\omega_0 = 0.2$, and $\Delta\omega = 0.2$.

calculate the following value:

$$\text{IPR}_w = \sum_{i,\mathbf{k}} |\tilde{v}_i(\mathbf{k})|^4, \quad (\text{S18})$$

where $\tilde{v}_i(\mathbf{k})$ is the Fourier component of the i th component of the Lyapunov vectors corresponding to the wavenumber \mathbf{k} . Supplementary Figure S15 presents the IPRs of the Lyapunov vectors in the wavenumber space. We find that the first and last 10 percents of the Lyapunov vectors exhibit large IPRs in the wavenumber space, while the others exhibit small IPRs. We note that the Lyapunov vectors corresponding to the small Lyapunov exponents also exhibit large IPRs in the real space. The Lyapunov vectors exhibiting large Lyapunov exponents and large IPRs in the wavenumber space should belong to a different class from the other bulk-extended ones.

The large IPRs in the wavenumber space are related to the band structure of the effective Hamiltonian obtained from the linearization of the equations of motion (see Supplementary Fig. S14). The bulk modes with large positive imaginary parts of eigenenergies are concentrated around the wavenumber $k_y = 0$. Therefore, we can describe the Lyapunov vectors corresponding to the large Lyapunov exponents as superpositions of the bulk modes only around $k_y = 0$, which leads to the large IPRs in the wavenumber space. We can discuss the large IPRs of some edge-localized Lyapunov vectors and the small IPRs of the other ones in a similar way.

Previous research of Hamiltonian chaos [57] has studied the participation ratio of coefficients of the eigenstates in a quantum chaotic system when they are described as the superposition of the eigenstates of decoupled harmonic oscillators. Such participation ratios classify the eigenstates in chaotic systems into regular and ergodic ones. In our model, the Lyapunov vectors exhibiting large (small) IPRs in the wavenumber space corresponds to regular (ergodic) ones. However, we leave the full understanding of the topological synchronized state in terms of Hamiltonian chaos to a future work.

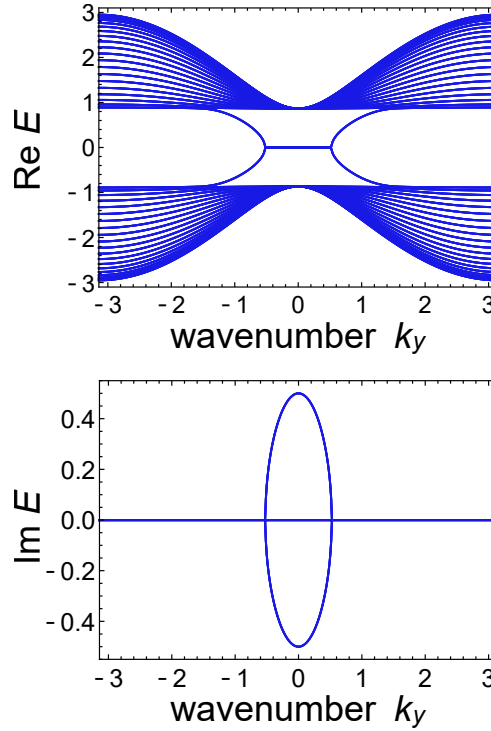


FIG. S16. Dispersion relation of the Hamiltonian of topological lasing modes. We calculate the dispersion relation of the Hamiltonian of topological lasing modes utilized in our model (Supplementary Eq. (S1)). We consider the open (periodic) boundary condition in the x (y) direction and arrange 20 sites in the x direction. We obtain doubly-degenerate gapless edge modes. Thus, the number of topological modes is four in this Hamiltonian, which is half of that in the state-dependent Hamiltonian. The parameter used are $u = -1$ and $b = 0.5$.

Dispersion relation of the Hamiltonian of a topological insulator laser

We compare the number of the gapless topological modes in the state-dependent Hamiltonian (cf. Fig. 5a in the main text) and the original Hamiltonian of topological lasing modes (Supplementary Eq. (S1)) utilized as the linear coupling in our first model. Here, we explicitly show the dispersion relation of the Hamiltonian of topological lasing modes without nonlinear loss terms. We consider the periodic boundary condition in the y direction. We arrange 20 sites and assume the open boundary condition in the x direction. We numerically diagonalize the Hamiltonian and obtain the dispersion relation shown in Supplementary Fig. S16. Since all the gapless modes are doubly-degenerated, there are four topological modes in this Hamiltonian. Meanwhile, the state-dependent Hamiltonian exhibits eight topological modes (note that the gapless modes in Fig. 5a in the main text are also doubly-degenerated). Therefore, the nonlinearity-induced on-site loss increases the number of topological boundary modes in the state-dependent Hamiltonian.

Absence of synchronized pattern in a topologically trivial system

The synchronization pattern discussed in Fig. 6 in the main text requires the topology of linear coupling. To clearly demonstrate this, we simulate the dynamics of our first model (Eq. (1) in the main text and Supplementary Eq. (S1)) in a topologically trivial parameter regime where the linear couplings exhibit no edge modes. We set the parameter $u = -3$ (cf. Supplementary Eq. (S1)) and the other parameters to be equal to those used in Fig. 6 in the main text. Supplementary Figure S17 shows the frequencies and the indicators of order parameters in the nontopological parameter region. We can confirm that the frequencies of the oscillators around damped ones are close to those away from damped regions and the indicators of order parameters are

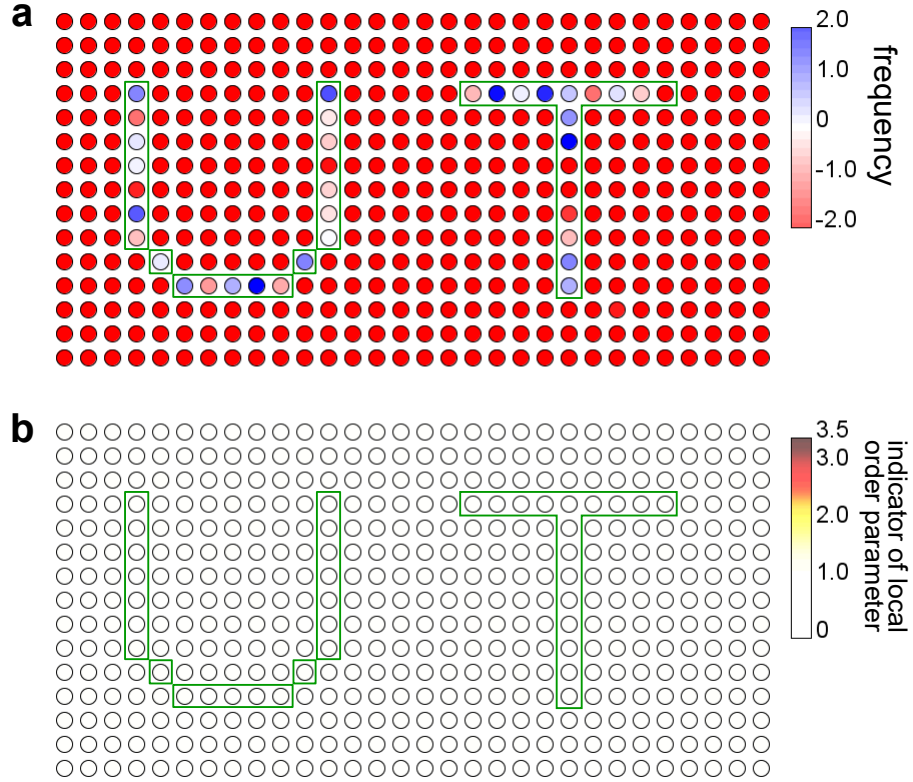


FIG. S17. Absence of synchronization pattern in a topologically trivial parameter regime. **a,b** We numerically simulate the first model of the TSS (Eq. (1) in the main text and Supplementary Eq. (S1)) in a topologically trivial parameter regime and confirm the absence of the TSS and its synchronization pattern. We damp the oscillators encircled by the green boxes. The parameters used are $u = -3$, $b = 0.3$, $\alpha = 0.5$, $\beta = 1$, $\omega_0 = 0.1$, and $\Delta\omega = 0.2$. **a** The frequency of the first component of the oscillator at each site at time $t = 200$ is depicted. The undamped oscillators exhibit inhomogeneous frequencies around -2.0 . **b** The indicator of the local order parameter of the first component of the oscillator at each site is shown. The indicator is small at every site, which indicates the absence of the synchronized oscillators.

small, which implies the absence of TSS. Therefore, the topology and edge modes of the linear couplings play a vital role in the synchronization pattern designing.

Circuit equation for realizing the TSS

Previous studies [48, 58–62] have proposed and realized topological edge modes in electrical circuits. The relation between the input current I_a and the electrical potential V_a at each node is described by Kirchhoff's law

$$I_a = \sum_b C_{ab}(V_a - V_b) + C_a V_a = \sum_b J_{ab} V_b, \quad (\text{S19})$$

where C_{ab} (C_a) is the inverse of the impedance between site a and b (site a and ground). iJ_{ab} plays the role of the effective Hamiltonian in electrical circuits. Resistors play the role of imaginary couplings, while capacitors and inductors lead to real terms in the effective Hamiltonian. By tuning the impedances of circuit elements, one can realize the effective Hamiltonian imitating topological materials. If we introduce capacitors with capacitance C as current resources, we can rewrite Supplementary Equation (S19) as

$$\frac{dV_a}{dt} = \frac{1}{C} \sum_b J_{ab} V_b, \quad (\text{S20})$$

which governs the time evolution of the voltage at each node.

To realize the electrical circuit of topological lasing modes, we utilize negative impedance converters with current inversion (ICINs), which is discussed in a previous study [48]. The ICINs realize nonreciprocal couplings ($C_{ab} \neq C_{ba}$) that cannot be realized by using resistors, inductors, and capacitors. Input current I_{in} and output current I_{out} are described as

$$I_{\text{out}} = \frac{1}{R}(V_{\text{in}} - V_{\text{out}}), \quad (\text{S21})$$

$$I_{\text{in}} = -\frac{1}{R'}(V_{\text{in}} - V_{\text{out}}), \quad (\text{S22})$$

where V_{in} (V_{out}) is the electric potentials at the input (output) side. We assume $R = R'$ in the electrical circuit of the TSS (cf. Fig. 8 in the main text). Then by tuning the parameters of circuit elements, one can construct the effective Hamiltonian iJ that is equal to the Hamiltonian of the topological insulator laser [40, 41] used in our first model (cf. Supplementary Eq. (S1)). It is noteworthy that impedances of capacitors and inductors and thus the effective Hamiltonian iJ depends on the driving voltage frequency.

To directly realize an electrical circuit whose voltage dynamics is described by nonlinear equations similar to our model, we next omit capacitors and inductors and construct a frequency-independent circuit of topological lasing modes. To effectively realize imaginary terms without capacitors and inductors, we prepare twice the number of nodes compared to the circuit in Fig. 8 in the main text and express one complex-valued state variable by using the voltages at two nodes as $Z = V_1 + iV_2$. Then, real and imaginary couplings are substituted as

$$CZ_j \rightarrow \begin{pmatrix} C & 0 \\ 0 & C \end{pmatrix} \begin{pmatrix} V_{j1} \\ V_{j2} \end{pmatrix}, \quad (\text{S23})$$

$$iCZ_j \rightarrow \begin{pmatrix} 0 & -C \\ C & 0 \end{pmatrix} \begin{pmatrix} V_{j1} \\ V_{j2} \end{pmatrix}, \quad (\text{S24})$$

where C is real. These real couplings are realized by the substitution of circuit elements shown in Fig. 8b in the main text.

Each node in the topological circuit of the TSS consists of van der Pol circuits [46, 47], which realize nonlinear oscillators. To construct the van der Pol circuits, we utilize nonlinear resistors whose conductance is described as $\tilde{C}(V_i)$. The dynamics of the van der Pol circuits is derived by Kirchhoff's law as

$$C \frac{dV_i}{dt} = \tilde{C}(V_i) V_i + I_{\text{in}}, \quad (\text{S25})$$

where C is the capacitance of the capacitor and I_{in} is the input current. When we can expand $\tilde{C}(V_i)$ as $\tilde{C}(V_i) = \alpha - \beta V_i^2 + \mathcal{O}(V_i^3)$, the dynamics of the van der Pol circuits can be approximated by the Stuart-Landau oscillators in the leading order. Therefore, the entire dynamics of the circuit imitates the first model of the TSS (Eq. (1) in the main text and Supplementary Eq. (S1)).

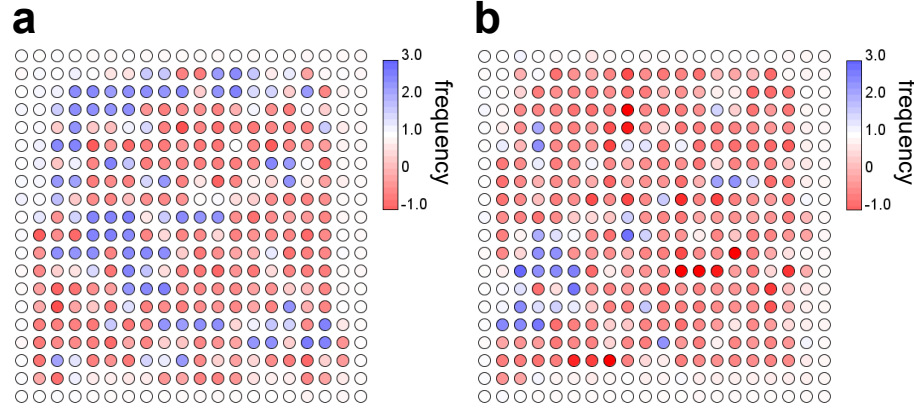


FIG. S18. Robustness of TSS against disorders in linear couplings. **a,b** We numerically simulate the model of the TSS (Eq. (1) in the main text) with the inhomogeneous linear couplings. Panel **a** (**b**) shows the frequency distribution at time $t = 100$ ($t = 200$). The edge oscillators exhibit homogeneous and constant frequencies, while the bulk ones oscillate at time- and space-varying frequencies. Therefore, we obtain the TSS robustly against the noise in linear couplings. The parameters used are $u = -1$, $b = 0.5$, $\alpha = 0.5$, $\beta = 1$, $\omega_0 = 1$, and $\Delta\omega = 0.2$.

Robustness of the electrical circuit realization of the TSS against spatial inhomogeneity of the circuit elements

TSS is robust against disorder due to its topological nature and thus is realizable without a fine-tuning of parameters. Especially, while there should be inhomogeneity in circuit constants of elements constructing the TSS circuit (cf. Fig. 8 in the main text), TSS remains stable against such disorders. To confirm the stability of TSS against the inhomogeneity of circuit constants, we numerically calculate the dynamics of our first model (Eq. (1) in the main text and Supplementary Eq. (S1)) under the fluctuating coupling strengths. We introduce the fluctuations of parameters corresponding to the inhomogeneous circuit elements by setting the proportion of deviation in the coupling strength from a site $(\mathbf{x}; a)$ to a site $(\mathbf{x}'; b)$ to be the same as that from a site $(\mathbf{x}'; b)$ to a site $(\mathbf{x}; a)$. We also consider the fluctuation of the parameters α and β in Eq. (1) in the main text, which is determined from the characteristics of the nonlinear current resources in the circuit of TSS (cf. Fig. 8 in the main text). We set the maximum width of these fluctuations as 10 percent of the mean values, and determine them as the distributions follow the uniform distribution. Supplementary Figure S18 shows the frequency distribution obtained from the simulation. One can confirm the emergence of the TSS, that is, the edge oscillators synchronize while the bulk ones exhibit chaotic behavior. Therefore, the TSS is robust against the fluctuations of parameters in Eq. (1) in the main text, which should be of practical advantage to experimentally realize the TSS.

* sone@noneq.t.u-tokyo.ac.jp

- [53] Qi X. L., Wu Y. S., & Zhang S. C. Topological quantization of the spin Hall effect in two-dimensional paramagnetic semiconductors. *Phys. Rev. B* **74**, 085308 (2006).
- [54] Shimada, I. & Nagashima, T. A Numerical Approach to Ergodic Problem of Dissipative Dynamical Systems. *Prog. Theor. Phys.* **61**, 1605–1616 (1979).
- [55] Ginelli, F. et al., Characterizing Dynamics with Covariant Lyapunov Vectors. *Phys. Rev. Lett.* **99**, 130601 (2007).
- [56] Kotwal, T. et al., Active topoelectrical circuits. *arXiv:1903.10130* (2019).
- [57] Stratt, R. M., Handy, N. C., & Miller, W. H. On the quantum mechanical implications of classical ergodicity. *J. Chem. Phys.* **71**, 3311–3322 (1979).
- [58] Ningyuan, J., Owens, C., Sommer, A., Schuster, D., and Simon, J. Time- and Site-Resolved Dynamics in a Topological Circuit. *Phys. Rev. X* **5**, 021031 (2015).
- [59] Albert, V. V., Glazman, L. I., and Jiang, L. Topological Properties of Linear Circuit Lattices. *Phys. Rev. Lett.* **114**, 173902 (2015).
- [60] Lee, C. H. et al., Topoelectrical Circuits. *Commun. Phys.* **1**, 39 (2018).
- [61] Imhof, S. et al., Topoelectrical-circuit realization of topological corner modes. *Nat. Phys.* **14**, 925–929 (2018).
- [62] Ezawa, M. Non-Hermitian boundary and interface states in nonreciprocal higher-order topological metals and electrical circuits. *Phys. Rev. B* **99**, 121411 (2019).